Quaternary surface ruptures of the inherited mature Yangsan fault: implications for intraplate earthquakes in Southeastern Korea

Sangmin Ha[1,2], Hee-Cheol Kang[1,3], Seongjun Lee[1,4], Yeong Bae Seong[2], Jeong-Heon Choi[5], Seok-Jin Kim[5,6], Moon Son[1]

5   [1]Department of Geological Sciences, Pusan National University, Busan 46241, South Korea
[2]Department of Geography Education, Korea University, Seoul 02841, South Korea
[3]Institute of Geohazard Research, Pusan National University, Busan 46241, South Korea
[4]Department of Geotechnology & Infrastructure, Byucksan Engineering, Seoul 08380, South Korea
[5]Research Center of Earth and Environmental Sciences, Korea Basic Science Institute, Chungbuk 28119, South Korea
10   [6]Conservation Science Division, National Research Institute of Cultural Heritage, Daejeon, 34122, South Korea

Correspondence to: Moon Son (moonson@pusan.ac.kr)

Abstract. Earthquake prediction in intraplate regions, such as South Korea, is challenging due to the complexity of fault zones. This study employed diverse methods and data sources to detect Quaternary surface rupturing along the Yangsan Fault to improve seismic hazard assessment. Paleoseismic data were analyzed to reveal insights into seismic activity,

15   displacement, and structural patterns. Observations from five trench sites indicate at least three faulting events during the Quaternary, with the most recent surface rupturing occurring approximately 3,000 years ago. These events resulted in a cumulative displacement of 3.1–94.0 m and maximum estimated magnitude of 6.7–7.2. The average slip rate of 0.14 mm/yr suggests a quasi-periodic model with possible recurrence intervals exceeding 10,000 years. The structural patterns imply the reactivation of a pre-existing fault core with top-to-the west geometry, causing a dextral strike-slip with a minor reverse

20   component. This study underscores the continuous faulting along the inherited mature fault, the Yangsan Fault, since at least the Early Pleistocene, contributing valuable insights for seismic hazard assessment in the region and offering a broader understanding of intraplate earthquake dynamics for earthquake prediction.

Short summary. Unlike episodic plate boundary earthquakes, their randomness makes predicting intraplate earthquakes

25   challenging. This study aids seismic hazard assessment by analyzing paleoearthquake records of the Yangsan Fault in Korea. Five trench sites revealed three Quaternary surface-rupturing earthquakes, the latest 3,000 years ago, with M_w 6.7-7.2. The right lateral fault has a 0.14 mm/yr slip rate, and a recurrence interval over 10,000 years, continuously active since the Quaternary.

1 Introduction

Earthquake prediction is challenging, and large earthquakes with surface ruptures significantly damage infrastructure (Geller et al., 1997; Wyss, 1997; Crampin and Gao, 2010; Woith et al., 2018). To predict large earthquakes, it is necessary to identify the pattern of earthquake occurrences, which can be periodic, quasi-periodic, and random (Shimazaki and Nakata, 1980; McCalpin, 2009). Earthquakes can be categorized as interplate (plate boundary) or intraplate (mid-continental) based on their

35   tectonic location (England and Jackson, 2011; Liu and Stein, 2016). Numerous studies have identified relatively "predictable" cycles, patterns, causes, magnitudes, and epicentres in the interplate, where earthquakes are more frequent, leading to improved earthquake preparedness (e.g., San Andreas Fault, Nankai trough; Powell and Weldon II, 1992; Murray and Langbein, 2006; Smith and Sandwell, 2006; Uchida and Burgmann, 2019; Obara and Kato, 2024).

Large earthquakes in the intraplate occur less frequently than in the interplate but can have devastating impacts (e.g., 1556

40   Huaxian earthquake-M 8.0, 1976 Tangshan earthquake-M_w 7.8, 1811-1812 New Madrid earthquake, 2001 Gujarat earthquake-M_w 7.6, 2011 Virginia earthquake-M 5.8; Min et al., 1995; Johnston and Schweig, 1996; Hough et al., 2000; Hough and Page, 2011; Wolin et al., 2012). Large intraplate earthquakes have recently received considerable attention and researchers are attempting to understand them based on insights obtained from interplate earthquakes (England and Jackson, 2011; Liu and Stein, 2016; Talwani, 2017). However, intraplate earthquakes exhibit complex spatiotemporal patterns that do not follow

45   general interplate earthquake pattern models (Liu and Stein, 2016; Talwani, 2017). This can partly be explained by the poor catalogue due to their slow slip rates (<1 mm/year) and long recurrence intervals (>1,000 yr). The primary reason behind the difficulty in predicting intraplate earthquakes is due to fault zone complexity and far-field stress, resulting in irregular earthquake behaviour (Liu and Stein, 2016; Talwani, 2017).

To unravel the complexity of fault zones, it is essential to understand the geometry and internal structure of fault zone, along

50   with the relationship between geometry and the in-situ stress regime, fault kinematics controlled by structure, and the correlation of these kinematics with paleoseismic data. Korea, located on the intraplate, has experienced very few directly damaging earthquakes since instrumented seismic monitoring began. However, medium-sized earthquakes have caused damage to people near the epicentres and raised earthquake awareness (e.g., the 2017 Pohang earthquake; Kim et al., 2018). Despite calls for realistic earthquake preparedness, seismic research in South Korea still remains at an early stage compared

55   to neighbouring countries on plate boundaries, such as Japan and Taiwan. Basic seismic hazard assessment requires the acquisition of reliable paleoseismic data (Reiter, 1990; Gurpinar, 2005; McCalpin, 2009). The reduction of paleoseismic uncertainty necessitates an expanded dataset, which in turn demands a significant volume of data. Various methods can be employed to efficiently detect Quaternary faults and obtain reliable paleoseismic parameters. Although this need has been recognized, until recently, paleoseismology studies in Korea have mostly been based on a single trench, with a few exceptions

60   (e.g., Kim et al., 2023). Earthquakes in South Korea appear to follow a pattern of intraplate earthquakes (Kim and Lee, 2023). To unravel this pattern, it is necessary to collect paleoseismic data from multiple faults with Quaternary surface rupturing to complete the puzzle. In this study, we try to provide clues to the pattern of earthquake behaviour.

This study sought to trace the distribution of the Quaternary surface rupturing during the Holocene and obtain fundamental paleoseismic data. To achieve this, we applied multiple methods to identify traces of Quaternary faults with higher accuracy

65   and interpret a highly reliable paleoseismic synthesis from the obtained large amount of data (e.g., five trenches and about ~30 numerical ages). We focused on the Byeokgye section (study area; Kim et al., 2022) in the southern part of the northern Yangsan Fault, a major tectonic line in southeastern Korea, to create geologic maps and select trench sites through fieldwork. This study aims to reveal 1) robust paleoseismic data, filling gaps in prior surface rupture documentation, 2) Quaternary reactivation features of intraplate mature fault zones, and 3) the spatiotemporal surface rupturing pattern of the Yangsan Fault,

70   a significant tectonic feature in East Asia and Korea. The results of this study can be used as essential inputs for seismic hazard assessment and to understand the Quaternary faulting patterns of the Yangsan Fault, which is located intraplate.
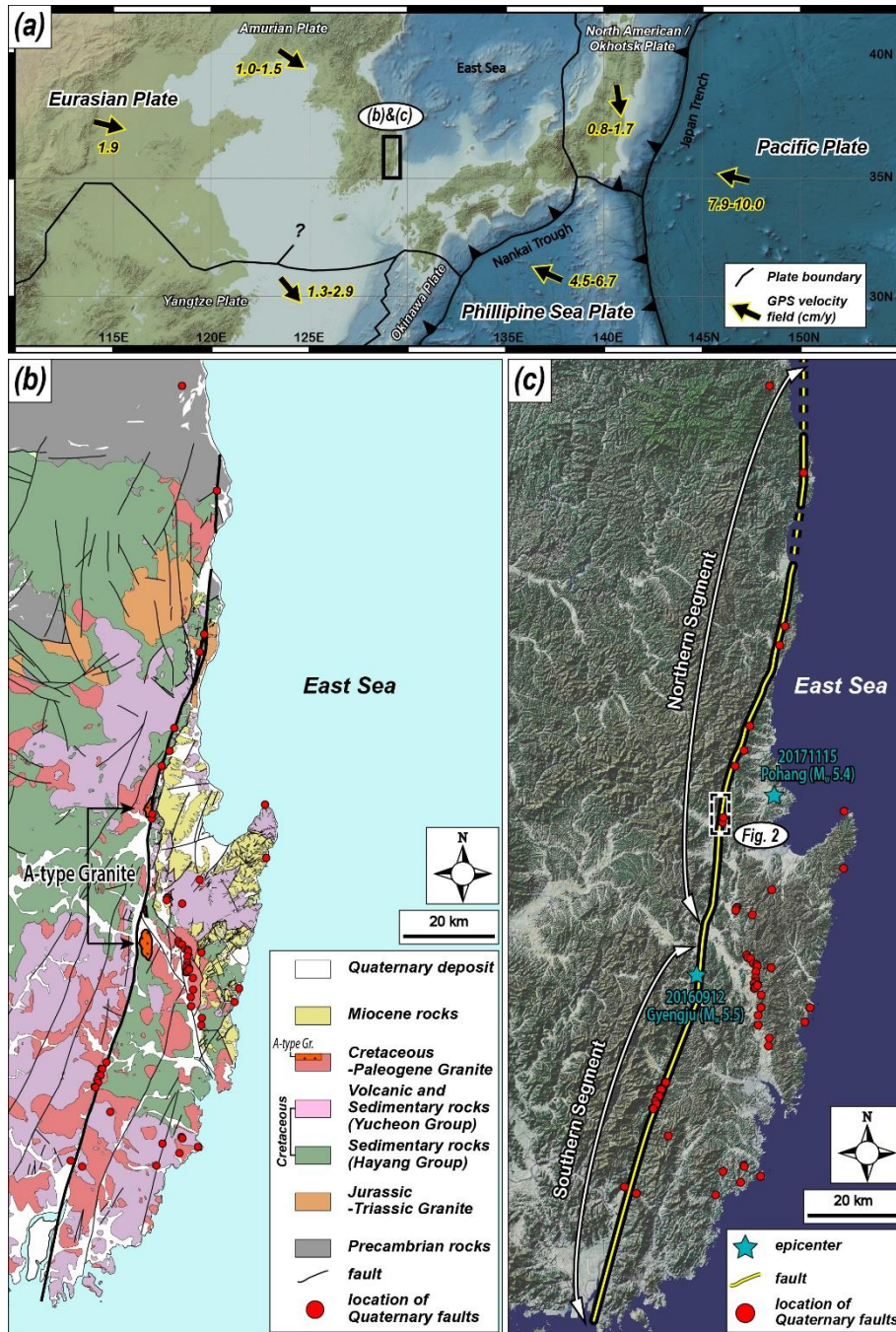
Figure 1: Regional study area maps. (a) Tectonic map of East Asia showing plate boundaries and their velocities (modified from DeMets et al., 1990, 1994; Seno et al., 1993, 1996; Heki et al., 1999; Bird, 2003; O'Nelli et al., 2005; Schellart & Rawlinson, 2010; M.-
75 **C. Kim et al., 2016). The black arrow indicates the moving direction of each plate. (b) Regional geological map of SE Korea (modified from Chang et al., 1990; Kim et al., 1998; Hwang et al., 2007a, 2007b; Son et al., 2015; Song, 2015; Kang et al., 2018). The thick black line indicates the Yangsan Fault and the 21 km dextral offset of the Yangsan Fault is interpreted by the distribution of a-type granite. (c) Topographic satellite image map of SE Korea and recent epicentres. The Yangsan fault is divided into two segments (modified from Kim et al., 2022; 2023b) and the study area located in southern part of the northern segment.**

2 Seismotectonic setting

2.1 Regional seismotectonic setting

The Korean Peninsula is located on the Amurian Plate, which was once thought to be part of the eastern margin of the Eurasian Plate (Fig. 1a; e.g., Bird, 2003; Calais et al., 2006; Argus et al., 2010; Ashurkov et al., 2011). The relative frequency of earthquakes in Korea is low compared with other countries on nearby plate boundaries, such as Japan, China, Taiwan, and the Philippines (KMA, 2022). While paleoseismology, archaeoseismology, and historical seismicity studies indicate that large (M≥7) earthquakes occurred in the past, medium-sized (M≥5) instrumental earthquakes have been consistently observed since the onset of seismic instrument measurements (Lee, 1998; Lee and Yang, 2006; Han et al., 2016; Kim et al., 2016; 2018; 2020b). Currently, the Korean Peninsula is under maximum horizontal stress in the E-W to ENE-WSW direction, which is the result of the combined effects of the subduction of the Pacific Plate and the far-field stress from the collision of the Indian and Eurasian plates (Park et al., 2006; Kim et al., 2016). GNSS studies show that the Korean Peninsula has a velocity field of about 3 cm/yr in the WNW direction (Ansari and Bae, 2020; Sohn et al., 2021; Kim and Bae, 2023). Recent short-term (2 years) GNSS studies on the Yangsan Fault suggest that the fault appears to be stable, with blocks on both sides of the fault moving in the same direction and at the same displacement rate (Kim and Bae, 2023).

Paleoseismological studies on the Korean Peninsula since the 1990s revealed that the most Quaternary surface ruptures were propagated along major structural lines in the southeastern part of the peninsula, such as the Yangsan Fault, Ulsan Fault, and Yeonil Tectonic Line (Figs. 1b and 1c; Kee et al., 2009; Kim et al., 2011; Choi et al., 2012; Kim et al., 2016). Since the 2016 Gyeongju earthquake, the Yangsan Fault has drawn increasing research attention in various fields, including tectonic geomorphology (Lee et al., 2019; Park and Lee, 2018; Kim and Oh, 2019; Kim et al., 2020d; Kim and Seong, 2021; Hong et al., 2021), structural geology (Woo et al., 2015; Choi et al., 2017; Cheon et al., 2017, 2019, 2020a; Kim et al., 2017a, b, 2020a, 2021, 2022; Ryoo and Cheon, 2019; Kwon et al., 2020), paleoseismology (Lee et al., 2015; Choi et al., 2019; Cheon et al., 2020b; Ko et al., 2020; Kim et al., 2023), and fault chronography (Yang and Lee, 2012, 2014; Song et al., 2016, 2019; Sim et al., 2017; Kim and Lee, 2020, 2023). The reported Quaternary surface rupturing were reactivated along the pre-existing fault surface with various kinematics depending on the relationship between the stress field and the geometry of the pre-existing structure (Cheon et al., 2020a). The Yangsan Fault, one of the most significant structural lines on the Korean Peninsula, extends > 200 km and is several hundred meters wide, with a prevailing horizontal displacement of > 20 km (Choi et al., 2017; Cheon et al., 2017, 2019, 2020a, b). The Yangsan Fault underwent multiple deformations with various kinematic senses during the Cretaceous to Cenozoic (Fig. 1b; Chang et al., 1990; Kim, 1992; Chang and Chang, 1998; Chang, 2002; Hwang et al., 2004, 2007a, b; Choi et al., 2009; Cheon et al., 2017, 2019). The dextral horizontal displacement of the Yangsan Fault is approximately 25–35 km in the Cretaceous sedimentary rocks (Chang et al., 1990) and 21.3 km in A-type granite on both sides of the fault (Fig. 1b; Hwang et al., 2004, 2007a, b). The most reported evidence for slip sense of Quaternary surface ruptures along the Yangsan Fault indicate that they have been reactivated with transpressional dextral slip sense under E-W to ENE-

WSW oriented compressional stress fields (Kim et al., 2011; Choi et al., 2012; Jin et al., 2013; Yang and Lee, 2014; Lee et al., 2015; Kim et al., 2016; Choi et al., 2019; Cheon et al., 2020a).

2.2 Geological settings of the detailed study area

The rocks in the study area are composed of Cretaceous sedimentary, volcanic, granitic, Paleogene alkaline granite, Middle Miocene sedimentary, and Quaternary sediments (Fig. 2a). Alkaline granite, used as a dextral offset marker for the Yangsan Fault, is distributed on the west side of the Yangsan Fault zone in the center of the study area and on the east side in Gyeongju and the offset is 21.3 km (Fig. 1b, Hwang et al., 2004, 2007a, b). The Middle Miocene sedimentary rocks in the eastern part of the study area are bounded by faults consisting of normal to dextral transfer faults, which form the western boundary of the Pohang Basin (Middle Miocene; Fig. 2a; Son et al., 2015; Song, 2015). Quaternary sediments in the study area are widely distributed along streams and valleys, and stratigraphic features cut by Quaternary faulting of the Yangsan Fault are observed in some places (Figs. 2b and 2c).

In the study area, the Byeokgye (outcrop) and Dangu (trench) sites have been reported as Quaternary surface ruptures (Fig. 2; Ryoo et al., 1999; Kee et al., 2009; Choi et al., 2012; Lee et al., 2015). The NNE-striking fault surface identified at the Byeokgye site cut the Cretaceous acidic and Quaternary sediments. Based on the shear bands within the fault gouge, drag folds in the footwall, and sub-horizontal striations, it was interpreted that strike-slip occurred after reverse slip (Ryoo et al., 1999). The most recent earthquake (MRE) of Byeokgye occurred after 7.5±3 ka, the optically stimulated luminescence (OSL) age of the truncated Quaternary sediments. Dangu is a trench approximately 50 m north of Byoegye that was excavated to obtain more detailed paleoseismic data (Lee et al., 2015). A fault surface (N10–20°E/75–79°SE) with geometric and kinematic characteristics similar to those of Byeokgye was found in the two trenches. The drag fold, slickenline, and three fault gouge zones observed in the cross sections indicated that at least three strike-slip events with reverse slip occurred after the deposition of Quaternary sediments. In addition, the MRE of Dangu using OSL dating, radiocarbon, and archaeological interpretation of artifacts in the Quaternary sediments is 7.5±3 ka (Lee et al., 2015). Recently, Song et al. (2020) excavated a trench 1 km north of Byeokgye to identify Quaternary faults and attempted paleoseismological interpretation. We set this trench as Trench 1 for a comprehensive interpretation and summarize the results.
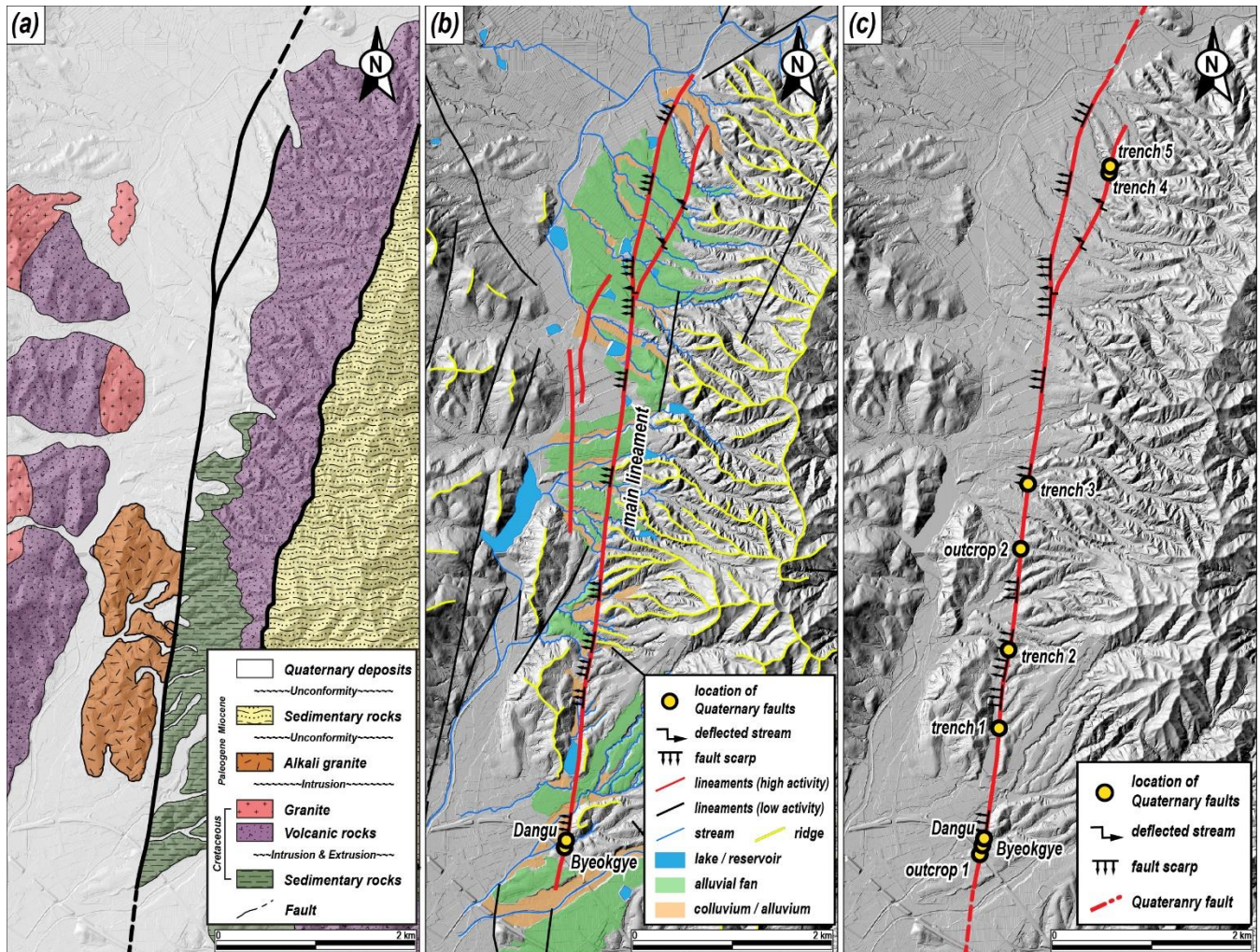
Figure 2: Detailed study area maps. (a) Geological map of the study area (modified from Hwang et al., 2007; Song, 2015). The alkali granite in the study area is used as a marker of YF's dextral offset. (b) Geomorphological map of the study area (modified from Ha et al., 2022). A fault trace is recognized as an array of fault scarps and deflected streams. (c) Fault trace map of the study area. Two outcrops and five trenches are located in the fault trace.

3 Method

3.1 Fault surface rupture tracking and trench siting

Ha et al. (2022) reported a 7.6 km fault trace in the study area through detailed topographic analysis using high-resolution (<< 20 cm) LiDAR images (Fig. 2b). They interpreted the main lineament as a fault scarp with a vertical displacement of 2–4 m and a dextral refraction channel with a horizontal displacement of 50–150 m. In the trench on the fault trace, the fault surface cuts through Quaternary sediments, indicating that the fault trace is Quaternary. We conducted fieldwork along this fault trace, trenched it at four sites, and identified two natural exposures.

3.2 Numerical dating

150 ### 3.2.1 Quartz OSL and K-feldspar IRSL dating

For luminescence dating, a total of thirty-six samples were collected from the trench section by inserting light-tight stainless-steel pipes (30 cm long and 5 cm diameter) into sand-rich layers. The sediment samples were then brought into a subdued darkroom to extract pure quartz and K-feldspar grains. The size fractions of 90–250 μm were first separated by wet sieving. Subsequently, these fractions were treated with 10% HCl (~ 1 h) and 10% H_2O_2 (~ 3 h) to remove carbonates and interstitial
155 organic matter. This was followed by density separation using SPT (sodium polytungstate; ρ=2.61 g/cm^3). Pure quartz and K-feldspar extracts were finally prepared by etching the sinking (quartz-rich) and floating (K-feldspar-rich) portions with ~ 40 % and 10% HF (~ 1 h), respectively. The extracts were then rinsed with 10% HCl to dissolve any fluoride precipitates that may have formed during HF etching. The purity of quartz extracts (i.e., the absence of K-feldspar contamination) was determined by comparing infrared-stimulated luminescence (IRSL) and blue-stimulated luminescence (BSL) signals using three natural
160 and beta-irradiated (20 Gy) aliquots. For all quartz extracts, the IRSL signals were negligible, with IRSL to BSL ratios well below 2 %, indicating that K-feldspar grains were effectively removed through the sample preparation procedure.

The luminescence signals were measured using a conventional Risø reader (Model TL/OSL-DA-20) installed at the Korea Basic Science Institute (KBSI). The stimulation light sources were Blue-LEDs (470 nm, FWHM 20 nm) for quartz and IR-LEDs (870 nm, FWHM 40 nm) for K-feldspar. The reader was equipped with a 90Sr/90Y source to deliver beta doses to the
165 sample position at a calibrated dose rate of 0.150 ± 0.002 Gy/s (Hansen et al., 2015). The signals were detected through a UV filter (U-340) for quartz OSL and blue filter pack (a combination of 4 mm Corning 7-59 and 2 mm Schott BG 39) for K-feldspar IRSL.

Quartz OSL equivalent dose (D_e) values were estimated using the single-aliquot regenerative-dose (SAR) procedure (Murray and Wintle, 2000), with preheat conditions for main regeneration and test doses of 260℃ for 10 s and 220℃ for 0 s,
170 respectively. Quartz OSL signals in dose saturation (i.e., for samples older than datable age ranges of quartz OSL dating method) and K-feldspar post-IR IRSL signals, which are well known to have higher dose saturation levels than quartz OSL (Buylaert et al., 2012), were used as samples for De estimation. K-feldspar post-IR IRSL De values were estimated using the SAR procedure suggested by Buylaert et al. (2009) where, after preheating at 250℃ for 60 s, IRSL signals in K-feldspar were read at 225℃ for 100 s, immediately followed by lower temperature (50℃) IR stimulation (Hereafter, this signal is referred
175 to as pIRIR$_{225}$). The measured fading rates (g$_{2days}$) of the K-feldspar pIRIR$_{225}$ signals ranged from 0–2 %/dec and fading corrections were made using the R package 'Luminescence' (Calc_FadingCorr; Kreutzer, 2023) to derive final pIRIR$_{225}$ age estimates. The quartz OSL and fading-corrected K-feldspar pIRIR$_{225}$ ages are summarized in Table 2.

3.2.2 Radiocarbon dating

Radiocarbon dating was performed to obtain independent ages and to cross-validate the ages of the sediments. Eight charcoal
180 samples were collected from sediment profiles of trenches 1, 2, and 4 and analyzed using accelerator mass spectrometry at the

Beta Analytic Radiocarbon Dating Laboratory. The ^{14}C age was calibrated to calendar years using the OxCal 4.3 (Bronk Ramsey, 2017) and IntCal 20 (Reimer et al., 2020) atmospheric curves.

3.2.3 [10]Be-[26]Al isochron burial dating

Isochron-burial dating is a variation of conventional burial dating methods that constrains the time elapsed since the sediment
185   burial and has been widely used for dating the alluvial sediments of 0.2–5.0 Ma (Granger & Muzikar, 2001). The burial
duration was calculated from the difference between the initial [26]Al/[10]Be ratio at the time of burial and the measured ratio of
[26]Al/[10]Be (Balco & Rovey, 2008; Erlanger et al., 2012). Unlike traditional simple burial dating, which assumes that the initial
ratio is known or the same as the surface production ratio of 6.8, isochron-burial dating requires multiple samples with their
pre-burial histories (i.e., various initial ratios of [26]Al/[10]Be) to construct an isochron. The initial ratio of [26]Al/[10]Be of the samples
190   at burial depended on the erosion and production rates in the source basin. Thus, we assumed that all the analyzed samples
originated from the same basin under steady-state erosion. The pre-burial (i.e., inherited) concentrations of the gravel at the
time of burial accumulated with a surface production ratio of 6.8 so that it falls on a line in the plot of [26]Al-[10]Be (Lal, 1991;
Granger, 2006; Balco and Rovey, 2008). We used the conventional value of 6.8 for the surface production ratio of [26]Al/[10]Be
for the current study, which can vary depending on longitude, latitude, and altitude (Balco and Rovey, 2008). Without
195   considering the pre-burial exposure history, the measured nuclide concentrations of gravels at the same depth should fall again
on a line in the plot of [26]Al-[10]Be with a mean life ($\tau_{pb} = (1/ (\lambda_{26} - \lambda_{10}))$; ~ 2.07 Ma) because they have the same post-burial
production of [26]Al (C_{26}) and [10]Be (C_{10}). Thus, the postburial component can be treated as a constant so that it can be modeled,
and the initial ratio of [26]Al/[10]Be (R_{inh}) can be calculated as

$$N_{26} = (N_{10}R_{inh}e^{-t/\tau_{pb}} + C_{10}R_{inh}e^{t/\tau_{pb}} + C_{26}) \qquad (1)$$

200   The final time (t_b) elapsed since burial can be calculated from the decay of the initial isochron (R_{inh}) to the isochron of the
measured samples (R_m):

$$t_b = \tau_{pb} \ln(R_m/R_{inh}) \qquad (2)$$

3.2.4 ESR dating

ESR dating of fault rocks is a method used to derive the timing of faulting by measuring the ESR signal in the quartz of a fault
205   gouge (Ikeya et al., 1982; Lee & Schwarcz, 1994). In general, ESR dating has an age detection limit of up to several thousands
of ka (e.g., Lee and Yang, 2003) and is thus helpful for direct dating the timing of faulting. The ESR signal of quartz grains
can be reset when the fault surface is subjected to normal stress of more than 3 MPa and displacements of more than 0.3 m
(Kim and Lee, 2020; 2023). These conditions are usually easier to meet at a depth of more than ~100 m than at the surface.
Therefore, it is likely that ESR signals from fault gouges currently exposed at the surface were reset at depths and then brought
210   up to the surface (i.e., current position) via uplift. In addition, in the case that the ESR signals were not completely reset during
faulting, the ESR ages may indicate the maximum age of MRE.

3.3 Paleo-stress reconstruction

Palaeo-stress reconstruction of Quaternary faulting was conducted using fault-slip data from 23 slickenlines in cross-sections. The data were analyzed using Wintensor S/W (v.5.8.5; Delvaux & Sperner, 2003). The type of stress regime is expressed quantitatively using the R' value: R′=R (σ_1 is vertical), or 2-R (σ_2 is vertical), or 2+R (σ_3 is vertical); R=$(\sigma_2-\sigma_3)/(\sigma_1-\sigma_3)$ (Delvaux et al., 1997).

3.4 Displacement and earthquake magnitude estimation

The slickenlines of the main fault surface and the vertical separation of quaternary sediments in the trench section were used to determine the true displacement of the MRE and the displacement per event. Deriving the true displacement is challenging when exposed sections are inclined, markers are inclined, or the slip sense is not purely dip-slip or strike-slip (which is almost always the case). In addition, displacements based on fragmentary information, such as bedrock separation and thickness of Quaternary sediments, can be over- or underestimated by fault slip motion and the possibility of paleo-topographic relief cannot be ignored. Despite these uncertainties, fault displacement is a necessary factor in earthquake magnitude estimation and key paleoseismological information; therefore, the process of collecting or estimating fault displacement is indispensable in paleoseismology. Therefore, correlations based on vertical separation, marker dip angle, angle of outcrop cross-section, fault dip angle, rake of slickenline, etc. are important for estimating the true displacement of a fault (Fig. A1; Xu et al., 2009; Jin et al., 2013; Lee et al., 2017; Gwon et al., 2021). The method of using their relationship to find the true displacement is described in detail in Appendix A.

Variables used for earthquake magnitude estimation include average displacement (Kanamori, 1977), maximum displacement (MD; Bonilla et al., 1984; Wells and Coppersmith, 1994), surface rupture length (Bonilla et al., 1984; Khromovskikh, 1989; Wells and Coppersmith, 1994), rupture area (Wells and Coppersmith, 1994), and surface rupture length × MD (Bonilla et al., 1984; Mason, 1996). However, in Korea, where rupture traces are difficult to find, it is difficult to use surface rupture length or rupture area owing to large uncertainties. Thus, we used MD, which is relatively easy to obtain from outcrops and trenches and more reliable. Many previous studies in Korea have applied the empirical relationship of the MD-moment magnitude (M_w) presented by Wells and Coppersmith (1994) (Kyung, 2010; Kim & Jin, 2006; Jin et al., 2013; Lee et al., 2017). We also estimated the maximum earthquake magnitude by applying the MD obtained from the trench to the empirical formula. The rake of slickenlines on the fault surface that underwent Quaternary faulting averages 20° and strike-slip motion was dominant; therefore, we used a corresponding strike-slip fault type M_w-MD empirical relationship. In addition, we used the MD-surface rupture length (SRL) empirical relationship to determine the extent to which the derived MD differed from the true displacement.

4 Results

4.1 Characteristics of Quaternary faulting in the trench

4.1.1 Trench 1

Trench 1 was reported by Song et al. (2020) and Ha et al. (2022) and the findings are summarized as follows:

245   Trench 1 was located on the main lineament, approximately 1 km north of the Byeokgye site (Fig. 2c). Nine Quaternary sedimentary units and seven east-dipping splay slip surfaces (F1–F7) cutting the units were found in the E-W trending trench section (Fig. 3). The hanging wall of F6 is the western boundary of pre-existing fault core more than 2.5 m wide and the footwall of F6 is a 4 m thick Quaternary sedimentary unit overlying the alkali granite. The pre-existing fault core is divided into two zones based on whether it is related to rupturing. Fault core 1 had a 40 cm wide blue fault gouge cutting Quaternary

250   sediments and a weakly developed shear band within the fault gouge. Fault core 2, east of fault core 1, did not cut the Quaternary sediments and consisted of a brown to dark gray fault-brecciated zone and a fault gouge zone more than 2 m wide. White, light-grey, and dark-grey fault gouge bands developed anastomosingly within the fault-brecciated zone. Slickenlines, observed at the boundary of the fault-brecciated and fault gouge zones, indicate a dextral strike-slip. The stratigraphic features of the nine units are listed in Table 1, and there are two noteworthy observations: First, the triangular-shaped unit D has a light

255   brown sandy matrix with good sorting and roundness compared to the surrounding units, despite it is surrounded by the slip surfaces (Fig. 3). It indicates that unit D may have been captured by the horizontal displacement of nearby sediments during the faulting event. Second, various types of seismogenic soft-sediment deformation structures (SSDs) are developed in units E and G (Fig. 3, Fig. 10 in Ha et al., 2022). The orientations of slip surfaces ranged from N60°W to N28°E, changing from NW-to NE-striking to the east. The F6 fault (N01°E/69°SE) cut through unit B and the F7 fault (N28°E/86°SE) is terminated

260   in unit C. Each of F3–F5 cuts through units D, E, and F, respectively, and is terminated under unit C. F1 and F2 cut through units G, H, and I but not through unit F. The rakes of the slickenline observed on F6 measured 15–55°, indicating a dextral strike-slip with a reverse component. Three faulting events can be analyzed in terms of the geometry of the sediments and the kinematics of the slip surface.

OSL/pIRIR$_{225}$ ages are presented in Table 2. We also conducted ^{14}C and ESR dating on the trench. Three charcoal samples

265   (1803BYG-01-C, 1803BYG-02-C, and 1803BYG-03-C) were collected from unit E and one charcoal sample (1803BYG-04-C) was collected from unit I for radiocarbon dating. The results of samples 1803BYG-01-C and 1803BYG-02-C are 36,897–38,420 and 43,802-45,670 Cal yr BP, respectively (Table 3). However, the ages of these two samples were near the upper limit of the radiocarbon dates and were stratigraphically contradictory, with the lower layer being younger than the upper layer. The age of 1803BYG-03-C (7,675–7,821 cal yr BP) from the upper part of unit E was inconsistent with the OSL age (1803BYG-

270   10-O: ~164 ka). It is possible that liquefaction in unit E caused a disturbance in the sediments and that the radiocarbon and OSL dates do not indicate the exact depositional timing. In addition, the radiocarbon age of 41,955–43,292 cal yr BP for the sample from unit I was near the upper limit of the radiocarbon ages and was thus subject to error. In particular, it was younger than K-feldspar pIRIR225 (177±7 ka (1803BYG-07-O)) from unit H, making it unlikely that this age was indicative of the

depositional age of unit I. For ESR dating, 36 fault gouge samples were collected from fault core 2 adjacent to F7, and ESR

275   dating was performed on 10 of them (1810BYG-01 to 10-E) (Fig. 3). The dates of each sample are presented in Table 4. The

weighted average ESR ages of the samples from the same fault viscose band were 245±37 ka (1810BYG-02-E, 1810BYG-10-

E), 406±35 ka (1810BYG-01-E, 1810BYG-05-E, 1810BYG-06-E), 387±26 ka (1810BYG-04-E), and 335±53 ka (1810BYG-

04-E) (Table 4). Samples with dose-saturated ESR signals (1810BYG-03-E, -07-E, and -08-E) were excluded from the

weighted average age calculations. Considering the error, the timing of faulting events using ESR ages at these sites can be

280   determined to be 245±37 and 406±35 ka. The main fault surface cut unit B and the MRE using the OSL age of unit B was

>3.2±0.2 ka (1803BYG-06-O; Table 2, Fig. 3). The geometry and cross-cutting relationship between the Quaternary sediments

and the seven fault surfaces indicated that a pre-existing fault core was reactivated during the Quaternary, resulting in at least

three faulting events (Fig.3; Fig. 9 in Song et al., 2020): the first (antepenultimate earthquake, AE) occurring at <142±4 ka

(1803BYG-12-O), the second (penultimate earthquake, PE) at >17±1 ka (1803BYG-13-O), and the third at the MRE (Table

285   2, Fig. 3).
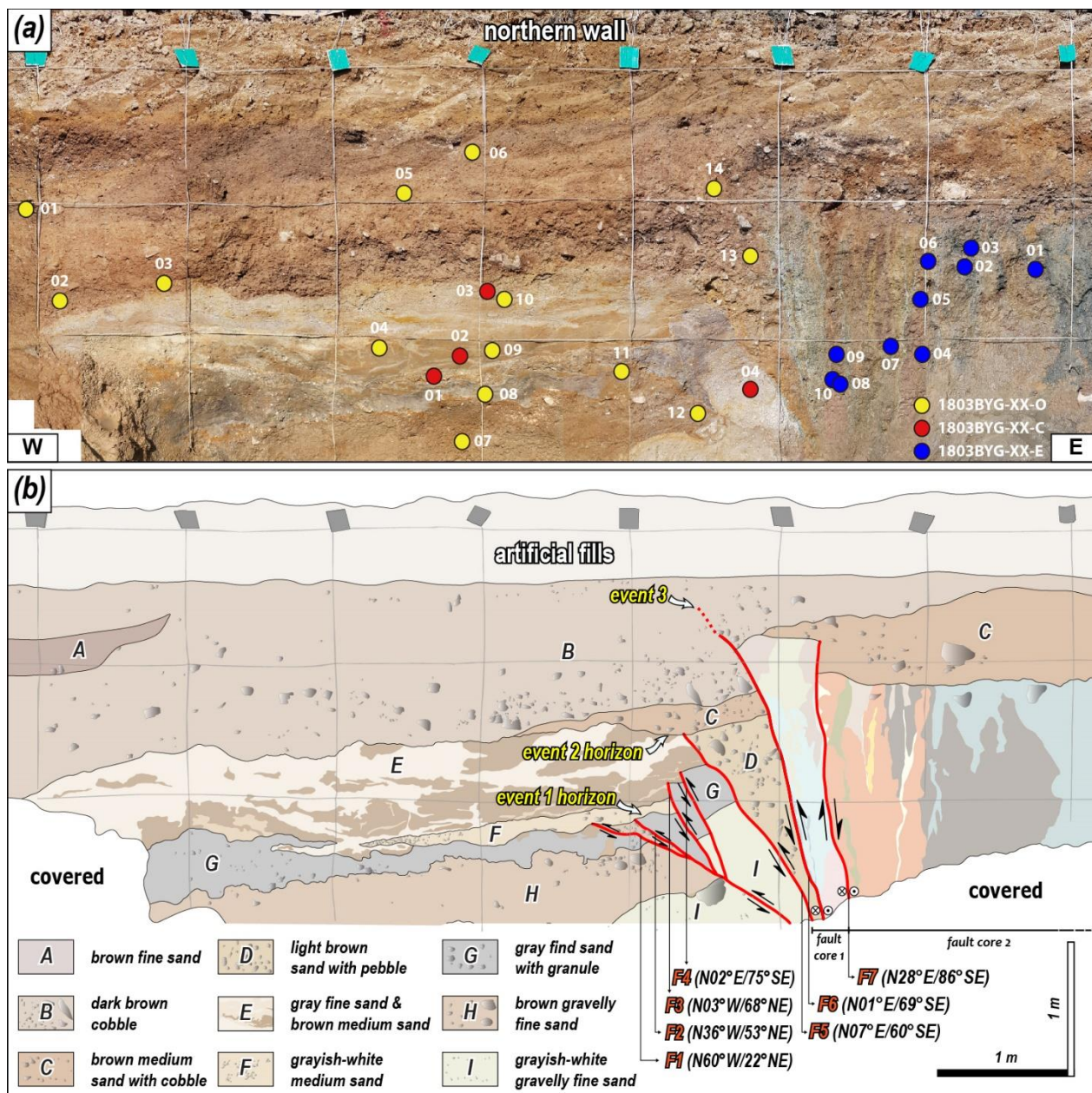
Figure 3: (a) Photomosaic of the trench 1 section of the northern wall. The colored circles represent samples for age dating. (b) Detailed sketch of the trench 1 section. Light grey lines indicate a 1 × 1 m grid.

290   **Table 1. Description of the units in each trench**

Unit	Trench 1	Trench 2	Trench 3	Trench 4	Trench 5
A	Brown fine sand, lens shape in unit B, coarsening upward in the bottom (silt to fine sand)	Reddish brown cobble deposits, A subangular clast composed of granitic and sedimentary rocks with a maximum diameter of 40 cm, poor sorting, charcoal in the bottom, cover the pre-existing fault core	Dark brown fine sand-silt	Brown fine sand, have a charcoal	Reddish brown pebble deposits, A subangular clast composed of granitic, sedimentary, volcanic rocks with a maximum diameter of 15 cm, good sorting, matrix-supported
B	Dark brown cobble, fine sand matrix, poor roundness, fining upward in clast (cobble to pebble) and matrix (sand to fine sand), the youngest unit cut by fault	Light grey silt-light yellowish brown fine sand, interbedded two layers, cut by main fault surface	Light brown boulder-cobble deposits, colluvial deposits from mountain slopes, moderate roundness, decreasing the clast size toward the west, cover the main fault surface	Dark brown cobble deposits-sand, colluvial deposits from mountain slopes, subangular clast, poor sorting, the youngest unit cut by fault	Reddish brown fine sand-slit, weak horizontal bedding, the youngest unit cut by fault, no truncation or deformation after MRE.
C	Brown medium sand with cobble, good roundness and sorting compared to unit b, pinch out in footwall, cover the pre-existing fault core		Brown pebble deposits, poor roundness and sorting, brown sand matrix, the youngest unit cut by fault	Light brown boulder deposits-sand, matrix is coarse sand to sand, angular clast, poor sorting, clast mainly composed of granite, the maximum diameter of a clast is ~ 120 cm	Reddish brown cobble-pebble deposits, fine sand matrix, clast composed of granitic, sedimentary, volcanic rocks, angular to sub-angular clast, poor sorting, containing clasts almost 40%. **Holocene ↑**
D	Light brown sand with pebble, good roundness and sorting despite adjacent fault, captured by a triangular shape, with fault surface		Yellowish-brown pebble deposits, colluvial wedge, triangular shaped, angular to subangular clast, poor sorting in bottom, fining upward, sand content increases with distance from the main fault surface	Brown sand-fine sand, fining upward	**Pleistocene ↓** Light bluish-grey pebble deposits, light grey fine sand matrix, the maximum diameter of a clast is ~ 20 cm, clast composed of sedimentary, volcanic rocks, angular to sub-angular clast, poor sorting
E	Gray fine sand & brown medium sand, mixing with gray and brown parts, SSDS (load structure dominated; load cats, pillar structure, sand dike, disturbed structure, structureless sediments)		Brown cobble-pebble deposits, subangular clast, poor sorting, intercalated fine sand to silt	Brown cobble deposits-coarse sand, alternating sand and gravel, average diameter of clast is 2-5 cm, subangular to angular, moderate sorting	Light yellowish brown pebble deposits, A slit near the fault surface gradually increases in grain size as it moves away, changing to a pebble deposit, angular to sub-angular clast, good sorting
F	Grayish-white medium sand		Brown sand-fine sand	Light brown sand-fine sand	
G	Gray fine sand with granule, SSDS (intrusive structure dominated; ball and pillow, flame structure, sand dike)		Brown pebble deposits, subangular clast, poor sorting, clast composed of granitic, volcanic, sedimentary rocks		
H	Brown gravelly fine sand, moderate roundness and sorting		Brown sand-fine sand		
I	Grayish-white gravelly fine sand, matrix derived from granite that basement rock				

Table 2. OSL/pIRIR$_{225}$ dating results

Trench number	Dating method	Sample number													
		01	02	03	04	05	06	07	08	09	10	11	12	13	14
Trench 1	OSL (ka)	1.3 ± 0.1	9.0 ± 1.0	10 ± 1		4.9 ± 0.3	3.2 ± 0.2							17 ± 1	8.1 ± 0.3
	pIRIR$_{225}$ (ka)				146 ± 8			177 ± 7	151 ± 8	143 ± 7	164 ± 8	155 ± 8	142 ± 7		
	Target unit	A	B	B	E	B	B	H	G	E	E	G	H	C	B
Trench 2	OSL (ka)					3.2 ± 0.3	3.4 ± 0.4	19 ± 1							
	pIRIR$_{225}$ (ka)														
	Target unit					A	A	A							
Trench 3	OSL (ka)										6.4 ± 0.4				
	pIRIR$_{225}$ (ka)		173 ± 6	175 ± 5					137 ± 3						
	Target unit		E	E					D		B				
Trench 4	OSL (ka)					1.3 ± 0.1	1.2 ± 0.1	0.15±0.01	0.15±0.01	5.9 ± 0.4					
	pIRIR$_{225}$ (ka)														
	Target unit					B	B	A	A	B					
Trench 5	OSL (ka)	10 ± 1	4.8 ± 0.2	2.8 ± 0.1	2.6 ± 0.1										
	pIRIR$_{225}$ (ka)														
	Target unit	C	C	B	B										

295

Table 3. ¹⁴C dating results

Sample name	Material dated	$\delta^{13}C$ (‰)	^{14}C age (yr)	Calibrated age (cal yr BP)[a]	Probability (%)[b]
1803BYG-01-C	Charcoal	-25.1	33400±220	38420-36897	95.4
1803BYG-02-C	Charcoal	-27.4	41250±500	45670-43802	95.4
1803BYG-03-C	Sediment	-24.7	6910±30	7821-7675	95.4
1803BYG-04-C	Charcoal	Not analyzed	38560±480	43293-41955	95.4
1810NSR-01-C	Charcoal	-27.8	170±30	0-291	95.4
1810NSR-02-C	Charcoal	-26.3	210±30	0-304	95.4
2009UGR-01-C	Sediment	-24.2	25230±100	29,576-28,966	95.4
2009UGR-02-C	Charcoal	-26.9	160±30	286-0	95.4
2009UGR-03-C	Sediment	-22.5	540±30	634-513	95.4

[a] Calibration used the database INTCAL13 (Reimer et al., 2013)

[b] Probability Method (Bronk Ramsey, 2009)

300 **Table 4. ESR dating results**

Trench	Sample number									
	01	02	03	04	05	06	07	08	09	10
Byeokgye	421±27	396±24	871±63	1886±319						
Trench 1	411±59	245±37	n.d.	387±26	406±35	403±63	n.d.	n.d.	335±53	248±40
Trench 2	790±60	409±41	405±32	n.d.	369±53	330±44	n.d.	n.d.	261±48	
Trench 3	425±66	409±52	702±123	n.d.						

n.d. = Not Determined

The details of all data are in Kim and Lee (2023)

4.2.2 Trench 2

Trench 2 was located on the main lineament 1.8 km north of the Byeokgye site (Fig. 2c). A low-angle fault surface
(N02°E/38°SE) cutting the Quaternary deposits was observed in the trench section (Fig. 4). The minimum 6-m-wide fault core
of the hanging wall was composed of mature fault rocks. The fault core was divided into fault cores 1 and 2 from the west,
with the yellowish-brown fault core 1 overlaying unit B (Fig. 4). Foliation developed within fault core 1, which abutted the
main fault surface in the upper part of the section. The strikes of the foliation within fault core 1 showed a wide range from
NE to E-W striking in shallow dip parts but were more consistently N-S or NNE striking where the dip increased. The main
fault surface that cut the Quaternary sediments showed a similar change from strike to foliation. The main fault surface had an
N-S strike in the lower part of the section and changed to an E-W strike as the dip became shallower. Toward the top of the
section, the dip deepened to regain the N-S striking. This indicated warping of the main fault surface along the pre-existing
structural grains and foliation (Figs. 4b and 4d). Fault core 1, without foliation, was a yellowish-brown fault-brecciated zone
composed of granitic rock breccia and a clayey matrix. The bluish-gray fault core 2 was bounded by a high-angle N-S striking
slip surface with fault core 1. The internal structure of the bluish-gray fault core was divided into four to six alternating gouge
and brecciated zones, each of which was bounded by an NNE- or N-S-striking slip surface. Numerous slickenlines (rake ≤ 10˚)
were observed on the slip surfaces in fault core 2, indicating dextral strike-slip movements. The main fault surface cut the
yellowish fault core and unit B and the slickenline revealed a dextral strike-slip with a reverse component. Unit A had a loose
matrix and relatively low consolidation compared to the underlying unit B and had an irregular boundary with the pre-existing
fault core (Table 1). At least one faulting event was identified on the cross-section, which did not reach unit A or the surface
(Figs 5c and 5d).

The OSL ages of unit A, which covers the fault, were 3.2±0.3 ka (1810NSR-05) and 3.4±0.4 ka (1810NSR-06) at the southern
wall and 19±1 ka (1810NSR-07) at the northern wall (Table 2). The radiocarbon ages of the charcoal in unit A were 0-291 and
0-304 cal yr BP (Table 3), making them much younger than the OSL age from unit A. Radiocarbon dates do not indicate when
the charcoal was deposited with the sediment but when the tree died after being rooted in the ground. The ESR ages obtained
from the fault gouge were higher than the depositional ages of the sediments cut by the fault (Table 4). The ESR ages suggest
that the quartz ESR signal in the fault gouge was not fully initialized during faulting. Therefore, we interpreted the faulting
event to have occurred after the ESR date of 261±48 ka (1810NSR-09-E). Taken together, these results indicate a depositional
age of 3.4±0.4 ka for unit A, which was not cut by the fault, and an ESR age for the fault gouge indicating a faulting event
after 261±48 ka, so the MRE of the fault in Trench 2 was interpreted to be before 3.4±0.4 ka.

To estimate the thickness of the Quaternary sediments and the cumulative vertical displacement of the fault, cored sediments
were sampled from the footwall along the main fault surface (Fig. C1). The Quaternary sediments extend to a depth of
approximately 32.8 m, underlain by a granite wash (1.2 m thick) of Paleogene alkali granite, and a subsequent fault damage
zone of the granite exists at its base (Fig. C1). Therefore, the vertical separation caused by Quaternary faulting in Trench 2
was at least 34 m. However, the vertical separation is a paleo-topographic relief difference that may have been caused by the

strike-slip movement of the fault. Cosmogenic ^{10}Be-^{26}Al isochron dating of the granite wash underlying the Quaternary sediments yielded a burial age of 2,871±593 ka, indicating that the thick Quaternary sediments started to be deposited after 2,871±593 ka (Table 5).
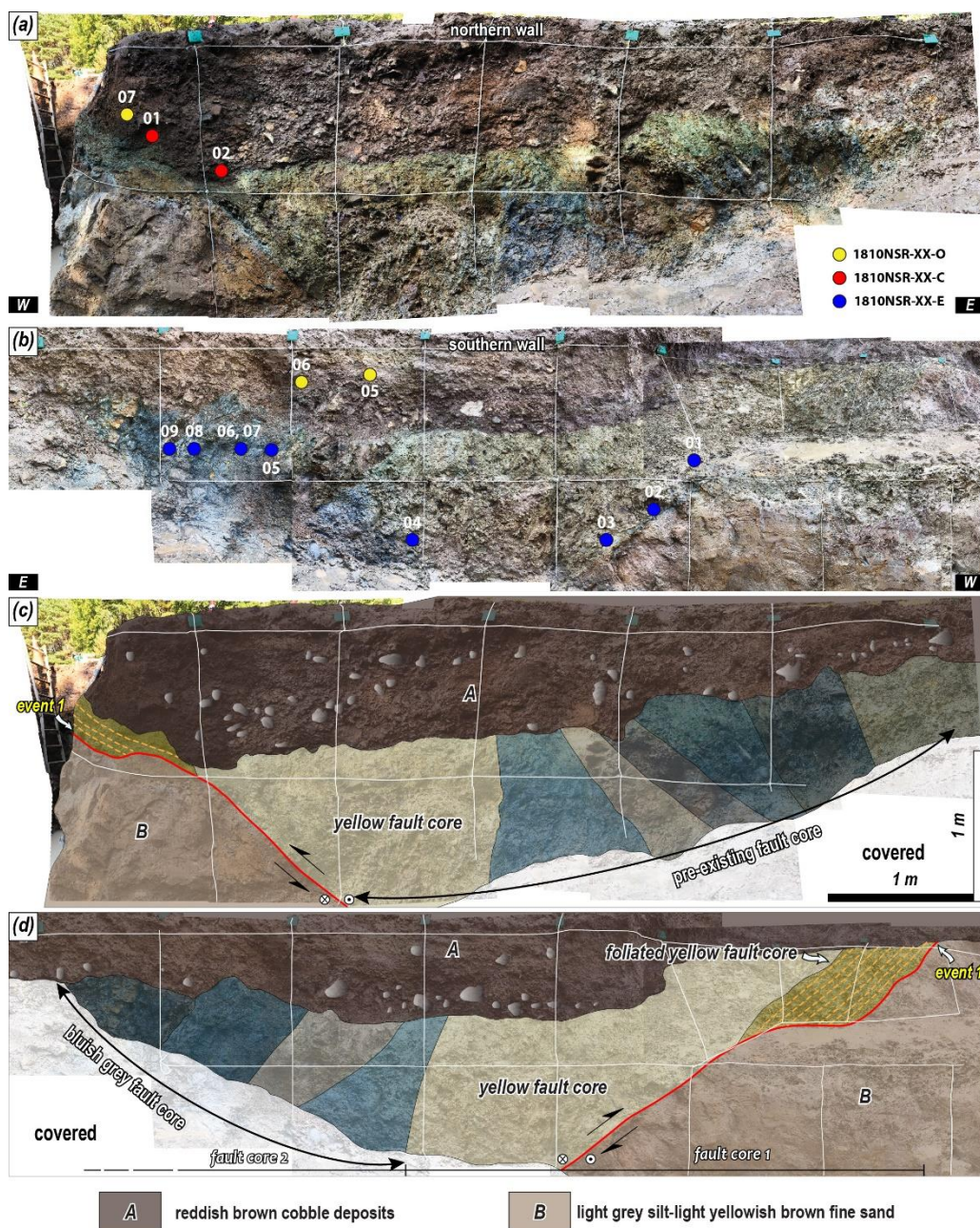
340 **Figure 4: Photomosaic of the trench 2 section of the (a) northern and (b) southern walls. The colored circles represent samples for age dating. Detailed sketch of the trench 2 section of the (c) northern wall and southern wall. White lines indicate a 1 m × 1 m grid.**

Table 5. Cosmogenic ^{10}Be-^{26}Al isochron burial dating results

Name	Latitude (˚N, DD)	Longitude (˚E, DD)	Elevation (m asl)	Depth[a] (m)	Density[b] (g·cm^{-3})	^{10}Be Conc. (10^4 atoms g^{-1})	^{27}Al Conc. (10^4 atoms g^{-1})	$^{26}Al/^{10}Be^c$	Isochron Age[d,e] (Ma)
NAN001	36.075519	129.256658	104	28	2.0	12.12 ± 0.53	23.39 ± 2.16	1.93	
NAN002	36.075519	129.256658	104	28	2.0	2.08 ± 0.08	6.89 ± 0.83	3.31	
NAN003	36.075519	129.256658	104	28	2.0	2.41 ± 0.10	10.39 ± 1.08	4.30	
									2.87 ± 0.59

[a] **Relative depth from the surface.**

[b] **Density of unconsolidated sediment.**

345   [c] **Production ratio for the surface is 6.75.**

[d] **Uncertainties are calculated at the 1σ confidence interval.**

[e] **All errors are propagated.**

4.2.3 Trench 3

Trench 3 was located on the main lineament extending 3.5 km north of the Byeokgye site (Fig. 2c). Eight Quaternary
350 sedimentary units and three fault planes were identified in the trench section (Fig. 5, Table 1). The hanging wall of the main
fault surface, which cut through Quaternary sediments, was composed of a pre-existing fault core. Excavation revealed a fault
core at least 20 m wide. The pre-existing fault core was divided into gouge and brecciated zones and the brecciated zone was
further divided into black-brown and gray by color. The fault gouge zone that cut the Quaternary sediments was narrower than
5 cm at the bottom of the section and widened to 40 cm at the top of the section; it was divided into an off-white fault zone
355 and a red fault zone by color and slip surface. The red fault gouge zone was almost entirely composed of clay; however, there
were numerous uncrushed quartz and rock fragments within the greyish-white gouge zone. The fault-brecciated zones were
all crushed, with numerous NE-striking veins embedded within the black-brown fault-brecciated zones. The slip surfaces
separating each zone within the fault core were all N-S- to NE-striking. The characteristics of the eight units are shown in
Table 1. Unit D was a colluvial wedge that indicates a paleo-earthquake (Fig. 5, Table 1). Brown sand to fine (units F and H)
360 and brown gravel (units C, E, and G) deposits were in the trench section. These features can be attributed to environmental
factors, such as deposition due to repeated rainfall, flooding, or seismic events due to repeated seismic motion. The slickenline
observed on the main fault surface indicates a dextral strike-slip with a small reverse component. There were at least two
estimated faulting events in this cross-section: event 1, which formed a colluvial wedge, and event 2, which cut the colluvial
wedge (Fig. 5).

365 The pIRIR$_{225}$ ages of sample 1903NR1R-02 and 03-O from unit E at the southern wall were 173±6 ka and 175±5 ka,
respectively, while the pIRIR$_{225}$ age of 1903NR1R-08-O from unit D, the colluvial wedge that directly indicated the timing of
the faulting event, revealed that the deposit formed at 137±3 ka (Table 2). Meanwhile, 1903NR1R-10-O from unit B, which
covered the fault, was dated as 6.4±0.4 ka. The youngest ESR age for the fault gouge was 409±52 ka (1903NR1R-02-E, Table
4). However, considering that the quartz ESR signal in the fault zone may not fully reset during faulting, this age implies that
370 the last faulting event occurred at or after 409±52 ka. The combination of descriptive features and ages suggests a paleo-
earthquake that formed the colluvial wedge at 137±3 ka, followed by MRE that cut the wedge between 137±3 and 6.4±0.4 ka.
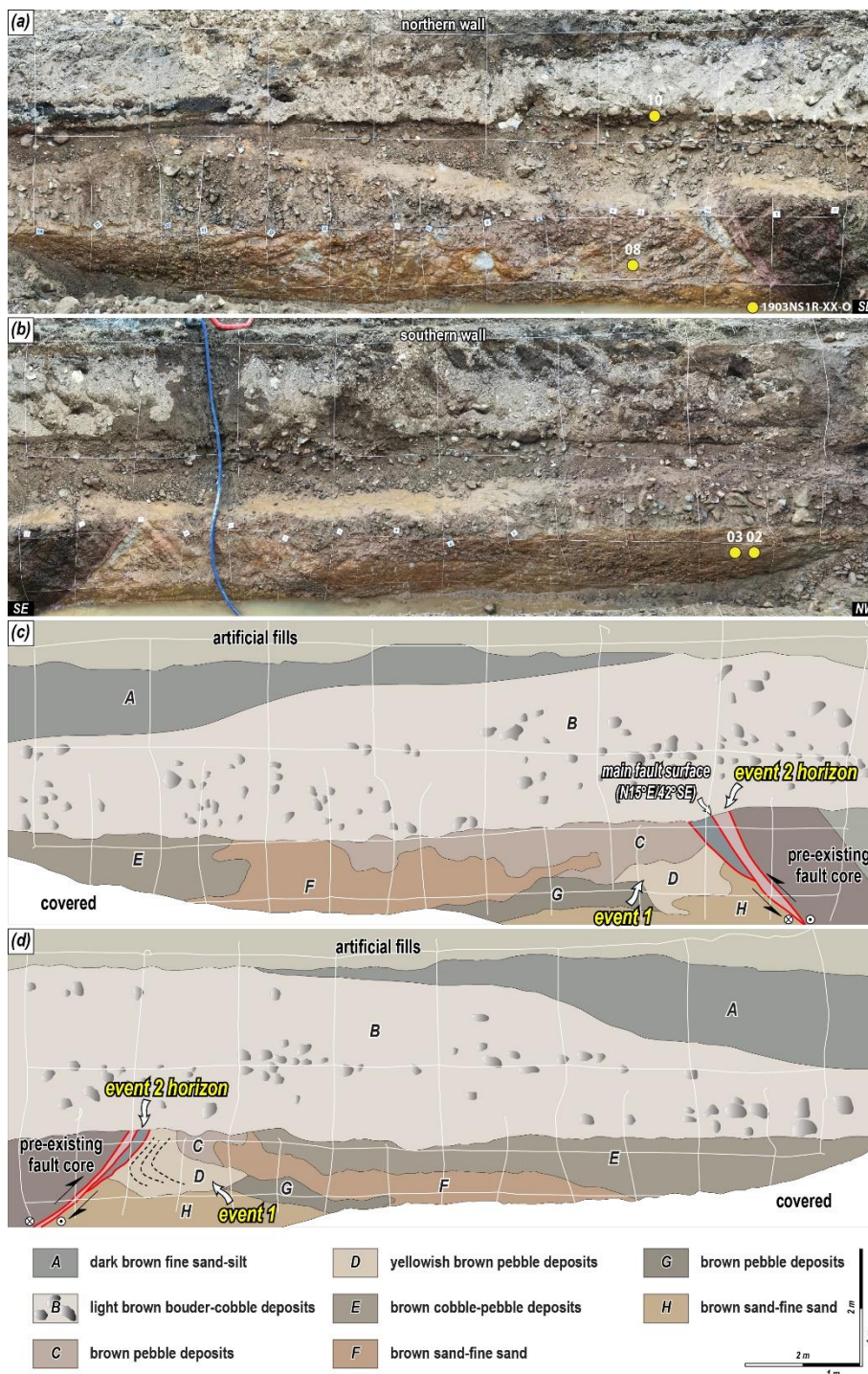
Figure 5: Photomosaic of the trench 3 section of the (a) northern wall and (b) southern wall. The colored circles represent samples for age dating. Detailed sketch of the trench 3 section of the (c) northern and southern walls. White lines indicate a 1 × 1 m grid. Black dot line reveals bedding trace.

4.2.4 Trench 4

Trench 4 was located on an NE-trending branch lineament from the main lineament that extends 6.3 km north of the Byeokgye site (Fig. 2c). In the trench section, there were five Quaternary sedimentary units cut by one main fault surface (Fig. 6, Table 1). The hanging wall of the main fault surface that cut the Quaternary sediments contained a pre-existing fault core that was at least 5 m wide during excavation. The pre-existing fault core was divided into two zones based on the color and type of fault rock. Fault core 1 is likely of alkaline granite origin and consisted of a reddish-brown gouge zone and a light-yellow breccia zone cutting through Quaternary sediments. The fault gouge zone was an equal mixture of gouge and breccia and the breccia was mostly composed of alkaline granite. In the area adjacent to the Quaternary sediments, a 20-cm-wide fault gouge zone developed, which was distinguished by yellowish-brown and reddish-brown gouges. The fault breccia zone was dominated by 30–50 cm alkaline granite breccias with dark gray to black fault gouges along both edges of the zone. Fault core 2, shown in gray, was dominated by a mixture of fault gouge and fault breccia. Slip surfaces of the N-S strike were developed within the fault core. In some sections within the fault core, a 30-cm-wide, dark gray fault gouge zone developed and the boundary of the fault gouge zone consisted of N-S striking slip surfaces containing slickenlines indicating dextral strike-slip. Units A and B showed horizontal to sub-horizontal bedding, whereas the bedding of units C-F tilted to the west, with dips of up to 50° adjacent to the main fault surface and becoming shallower toward the west (Fig. 6, Table 1). The difference in bedding indicated an angular unconformity between unit B and units C–F. The slickenline observed on the main fault surface indicates a dextral strike-slip with a small reverse component. At least two faulting events were inferred from the cross-section: event 1 (PE), which caused units C–F to tilt after they were deposited, and MRE, during the deposition of unit B, after an angular unconformity (Fig. 6).

We collected five samples from the northern wall of units A and B and four from units D and F for dating. The OSL age of 5.9±0.4 ka was 2009UGR-09-O, which was cut by the fault. For the remaining four samples that were not cut by the fault, the oldest OSL age was 1.3±0.1 ka, obtained for 2009UGR-05-O (Table 2). The fault event occurred during the continuous deposition of unit B. Samples were collected from units F (2009UGR-01-C) and A (2009UGR-02-C) for radiocarbon dating (Table 3). The radiocarbon age of the charcoal from 2009UGR-02-C was 160±30 cal yr BP, which agreed with the OSL age of 0.15±0.01 ka of the sediment containing the charcoal (2009UGR-07-O) and strongly indicated that unit A was deposited at this time. The MRE for this trench, derived from comprehensive dating analyses, indicates 1.3±0.1–5.9±0.4 ka.
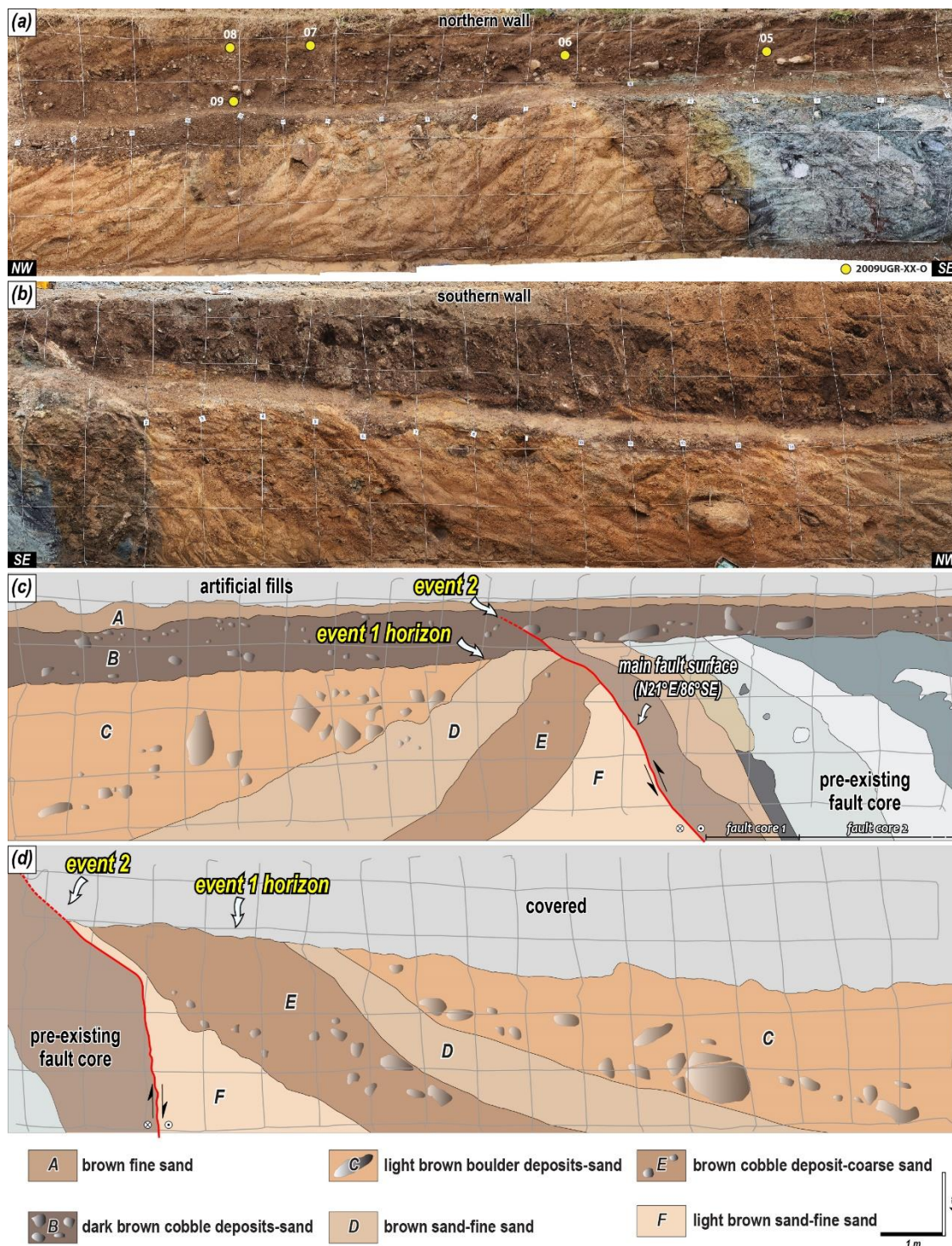
Figure 6: Photomosaic of the trench 4 section of the (a) northern and (b) southern walls. The colored circles represent samples for age dating. Detailed sketch of the trench 4 section of the (c) northern and southern walls. Grey lines indicate a 1 × 1 m grid.

4.2.5 Trench 5

Trench 5 was located 40 m north of Trench 4. The trench section contained five quaternary sedimentary units, cut by one main fault surface (Fig. 7). The overall appearance of the cross-section was similar to that of Trench 4. The hanging wall of the fault

410 that cut the Quaternary sediments consisted of a pre-existing fault core at least 20 m wide. The pre-existing fault core was derived from alkaline granite, as shown in Fig. 6. The fault core was divided into a fault gouge zone and a fault breccia zone bounded by an N-S to NNE striking slip surface. The host rock of the light-yellow fault breccia zone was interpreted as alkaline granite and contained a 5–10 cm wide black fault gouge. Where it abuts the Quaternary sediments, a 10 cm wide light gray fault gouge developed, which changed to a yellowish grey fault gouge with yellow clay mixed toward the top. A 20 cm-wide

415 fissure filling was unveiled near the main fault surface and the slip surface within the fault core showed multiple slickenlines, indicative of dextral strike slips. Compared to Trench 4, units A–C in Trench 5 were considered to have the same deposits as units A and B in Trench 4 and units D and E in Trench 5 were interpreted to have the same deposits as units C–F in Trench 4. Units D and E in Trench 5 showed westward-dipping bedding like units C–F in Trench 4, whereas units A–C had subhorizontal bedding. The reddish-brown sediments in the upper part of Trench 5 were thicker than those in Trench 4, indicating that a

420 more accurate MRE could be identified compared with Trench 4. The slickenline observed on the high-angle main fault surface indicated a dextral strike-slip with a small reverse component. The number of faulting events was estimated at least two based on the same angular unconformity as in Trench 4. Event 1 caused units D and E tilting, which cut them. Event 2 occurred during the deposition of unit C, which failed to cut into unit B.

The OSL ages of 2010UGR-03-O and 04-O from unit B on the south slope were 2.8±0.1 and 2.6±0.1 ka, respectively, and

425 those of 2010UGR-01-O and 02-O from the fault-cut unit C were 10±1 and 4.8±0.2 ka, respectively (Table 2). Trench 5 yielded a tighter MRE range of 2.8±0.1–4.8±0.2 ka than the MRE of Trench 4.
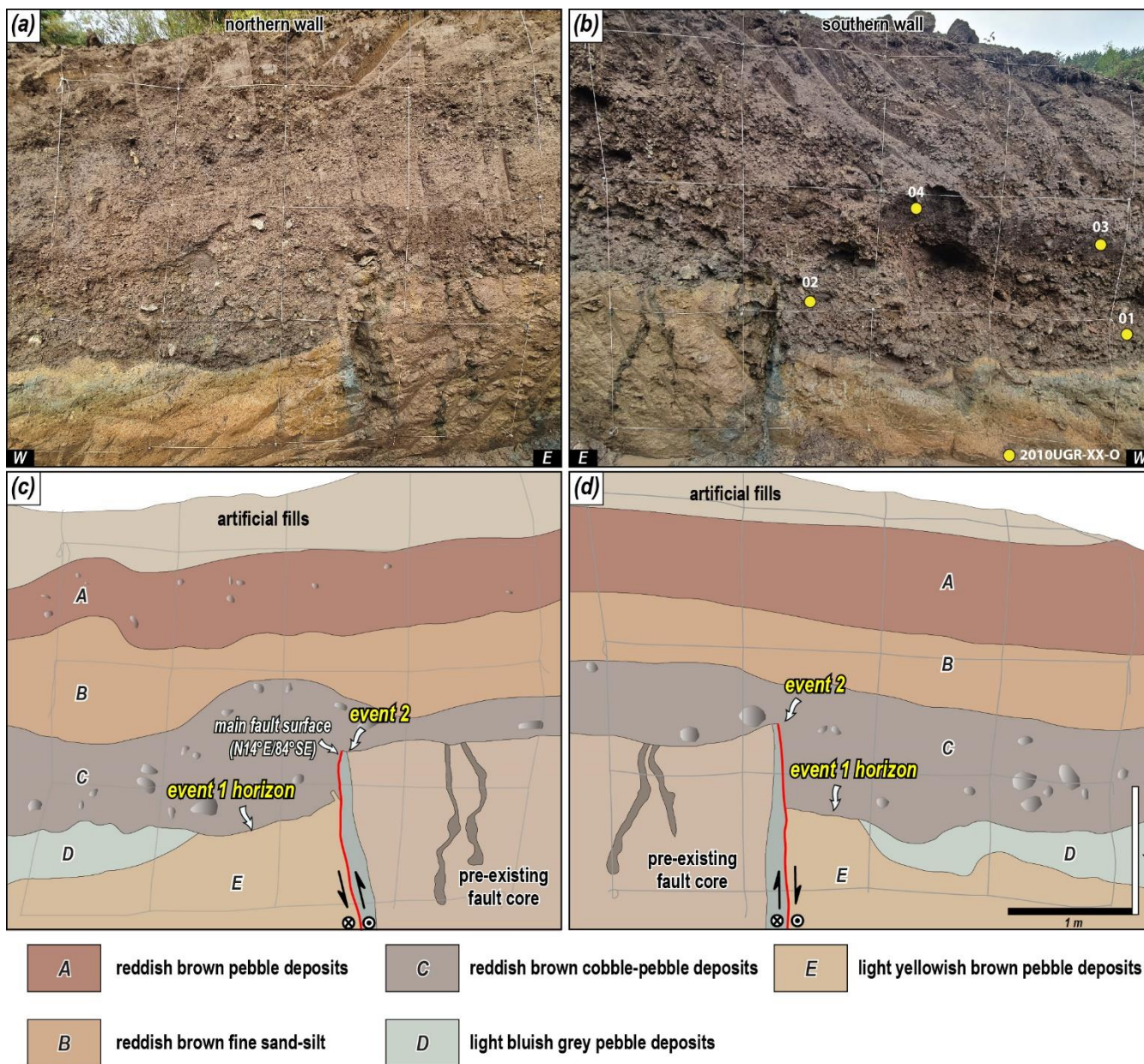
Figure 7: Photomosaic of the trench 5 section of the (a) northern and (b) southern walls. The colored circles represent samples for age dating. Detailed sketch of the trench 5 section of the (c) northern and southern walls. Grey lines indicate a 1 × 1 m grid.

430

4.3 Paleo-stress reconstruction

The slickenlines found in the trench were divided into those in the main fault surface that cut the Quaternary sediments and those in the pre-existing fault core. For the reconstruction of the paleo-stress field, twenty kinematic data along with the geometry of the fault planes and slickenlines were collected and analyzed using Wintensor S/W (v.5.8.5) (Delvaux & Sperner, 2003). Based on the slickenlines of the main fault surface, the analysis yielded a maximum horizontal stress (σ_{Hmax}) in the ENE-WNW direction (R´=1.62; Delvaux et al., 1997; Fig. 8), which agrees with the current stress field on the Korean Peninsula (Kim et al., 2016). The slickenlines in the pre-existing fault core indicated NE-SW compression, which was consistent with the stress field that causes dextral strike-slip deformation, which is one of the major movements of the Yangsan Fault (Cheon et al., 2019, 2020a). The reconstructed paleo-stress indicated that the dextral strike-slip with a small reverse component identified in the main fault surface occurred in an ENE-WSW compressional stress regime.
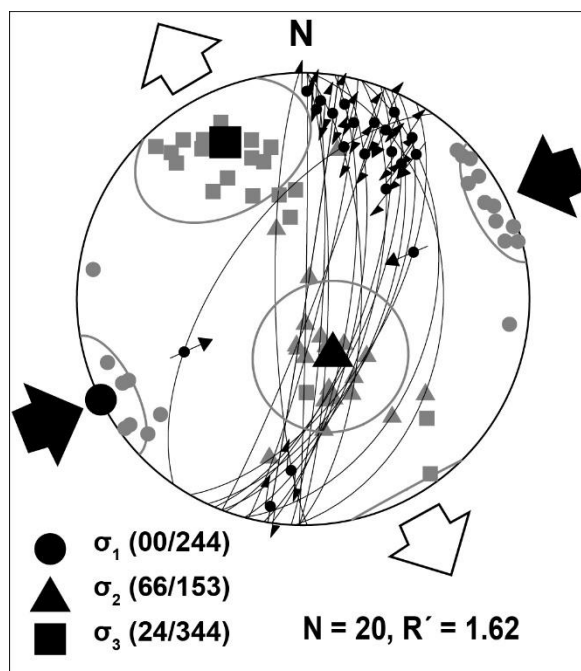
Figure 8: Fault slip data in the fault zone (lower-hemisphere, equal-area projection). Convergent and divergent arrowheads represent contraction (σ_{Hmax}) and horizontal stretching (σ_{Hmin}) directions, respectively. The principal stress axes σ_1 (circles), σ_2 (triangles), and σ_3 (squares) are projected. R´=2-R (σ_2 is vertical) [Delvaux et al., 1997; R=(σ_2-σ_3)/(σ_1-σ_3)].

4.4 Displacement and earthquake magnitude estimation

The results calculated using the marker, vertical separation of each trench, and Eq. (A1) are listed in Table 6. In our previous study, the true displacement of the MRE at the Dangu site was determined to be 2.64 m (Lee et al., 2016). For each faulting event in Trench 1, the displacement per event according to the event horizon was 0.33–1.81 m, the true displacement of the MRE was 0.61–2.81 m, and the cumulative displacement based on the unconformity of the bedrock and Quaternary sediments was 3.1–8.8 m. Using the bedrock and Quaternary sediments unconformity identified by corings in Trench 2 as a marker, the

cumulative true displacement was 94 m. The MRE cutting the colluvial wedge in Trench 3 had a true displacement of 3.29 m. However, when considering the overall interpretation, only the MRE and AE, but not the PE, are recognized in Trench 3 (Figs. 5 and 9). The displacement cutting the colluvial wedge likely reflects the displacement of the missing PE as well as the MRE, which is supported by the long interval between the wedge (unit D) and the deposit covering the wedge (unit B). Thus, it is

455   reasonable to exclude the calculated displacement as it is unlikely to be the displacement of the MRE. The true displacement of the MRE in Trench 4 and 5 was 0.86 m and 1.17–2.34 m, respectively, using the lower boundary of units B and C as markers. Combining the results from each trench, the true displacement of MRE in the study area was 0.64–2.81 m and the cumulative displacement was 3.1–94 m. The displacement per event was similar, between 0.33–1.1 m for PE and AE (event 1, 2), but the trench showed a higher displacement for the MRE (event 3).

460   We assumed the maximum earthquake magnitude by applying the MD (0.64–2.81 m) of the MRE. The maximum magnitude of the MRE was estimated to be 6.7–7.2. Furthermore, the surface rupture length (SRL) of 7.6 km obtained from the topographic analysis (Ha et al., 2022) was applied to the MD-SRL empirical relationship. The calculated MD was 0.21 m, which was smaller than the true displacement of the MRE (0.64–2.81 m), suggesting that the actual surface rupture length in the study area exceeds 7.6 km, although this was not confirmed by the current topography. The earthquake magnitude was

465   estimated from the seismic SSDs in the trench cross-sections (units E and G in Trench 1; unit F in Trench 3). In unit E, the clastic dike varied in size from approximately 20 to 50 cm, whereas in unit G, a ball-and-pillow structure of more than 30 cm developed (Song et al., 2020; Ha et al., 2022). Atkinson et al. (1984) reported that liquefaction phenomena, including SSDs above a certain size in sediments of shallow lake or fluvial origin, occur when the minimum earthquake magnitude exceeds 5.5. Based on this, the estimated earthquake magnitude of these SSDs structures may vary depending on the depositional

470   environment and substrate characteristics. However, it was estimated to be at least 5.5, which is consistent with the magnitude of the inferred empirical relationship.

Table 6. Fault displacement of study area

	Dangu[a]				Trench 1[b]				Trench 2				Trench 3				Trench 4				Trench 5			
	S_v (m)	α (°)	γ (°)	**S_t (m)**	S_v (m)	α (°)	γ (°)	**S_t (m)**	S_v (m)	α (°)	γ (°)	**S_t (m)**	S_v (m)	α (°)	γ (°)	**S_t (m)**	S_v (m)	α (°)	γ (°)	**S_t (m)**	S_v (m)	α (°)	γ (°)	**S_t (m)**
MRE	0.67	79	15	**2.64**	0.49	69	17-56	**0.64-1.81**					1.1	42	30	**3.29**	0.25	86	17	**0.86**	0.4-0.8	84	20	**1.17-2.34**
Marker	Unit D				Unit C								Unit D				Unit B				Unit C			
PE (event 2)					0.31	75	17-56	**0.39-1.1**																
Marker					Unit G																			
AE (event 3)					0.22	53	17-56	**0.33-0.94**																
Marker					Unit H																			
Cumulative displacement					2.4	69	17-56	**3.1-8.8**	34	38	36	**94**												
Marker					Quaternary deposit thickness																			

[a]**modified from Lee et al., 2015**

[b]**modified from Song et al., 2020**

5 Discussion

5.1 Interpretation of Paleoseismic data

5.1.1 MRE and number of surface faulting

We determined the MRE and number of faulting events of the study area based on each trench site, considering previous studies, the age of Quaternary deposits and fault gouges, the geometry and cross-cutting relationship between faults and sediments, and the kinematics in the trench section (see the heading 4.1). The results for each trench were synthesized to estimate the MRE, number of earthquakes (faulting events), and timing of earthquakes in the study area (Fig. 9). First, the MRE was 2.8 ± 0.1–3.2 ± 0.2 ka, which is the time of overlap in several trenches. Considering the error range, the surface rupture must have occurred approximately 3,000 years ago. Considering the minimum number of earthquakes estimated for each trench as the maximum, at least three faulting events may have occurred in the study area, as determined from the Dangu site and Trench 1. The timings of the remaining two prior earthquakes, excluding the MRE, were quantified by combining the age and interpretation of each trench. The penultimate earthquake (PE) occurred in 17 ± 1–75 ± 3 ka, which was determined using the youngest age of the PE (unit C) from Trench 1 and the MRE from the Byeokgye site (Fig. 9). The antepenultimate earthquake (AE) was from 137 ± 3–142 ± 4 ka, constrained by the age of the lowermost sediments cut by the fault in Trench 1 and the colluvial wedge in Trench 3. On the other hand, clustering the ESR ages at each trench with an error range suggested at least three separate earthquakes at 245 ± 37, 404 ± 10, and 817 ± 10 ka (Fig. 9). These ages indicate the time elapsed since the ESR signal was set to zero by the faulting at depth, but it needs much care to use as a timing indicator of the faulting event as the ESR signal was not completely bleached. Nevertheless, the faulting patterns recognized from clustering in several trenches indicated that the study area experienced at least three earthquakes in addition to those that cut Quaternary sediments.
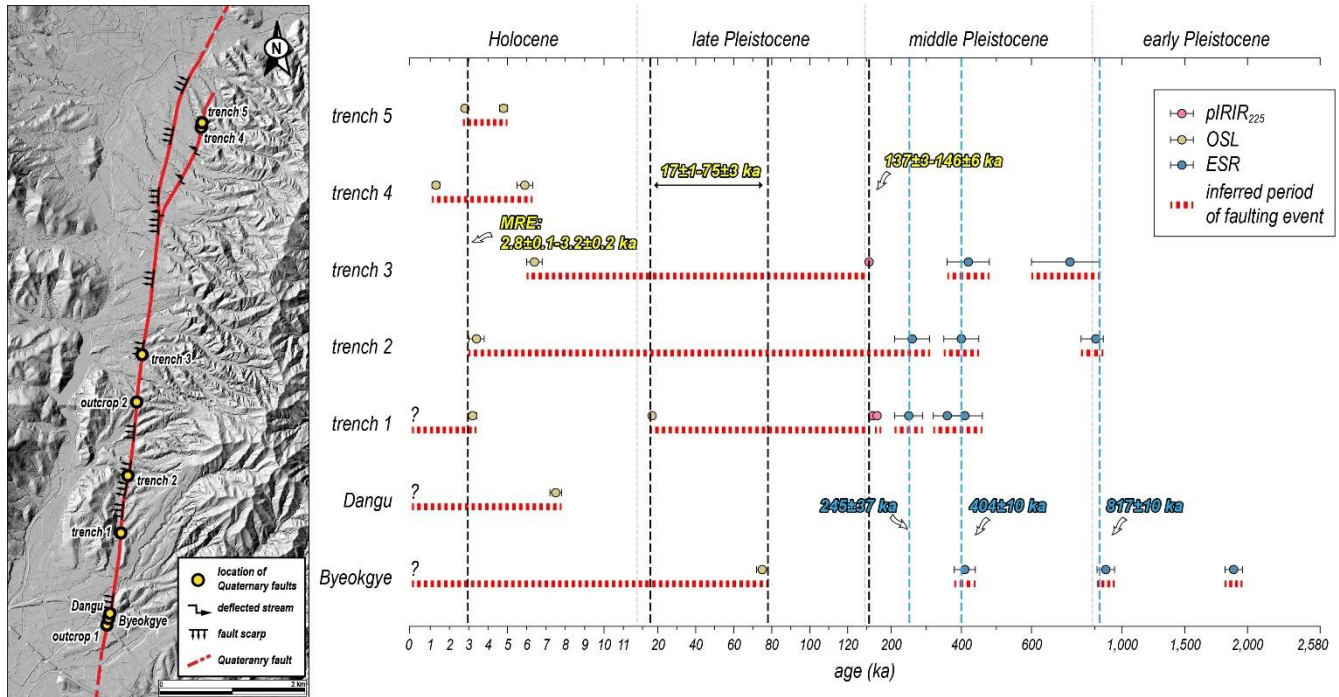
Figure 9: Age distribution graph of the study area. The graph reveals the timing of the paleo earthquake based on trench interpretation and age overlap. The most recent earthquake in the study area occurred probably around 3,000 years ago.

5.1.2 Quaternary slip rate and recurrence interval

The slip rate is an expression of the average displacement of a fault over a period, which numerically shows how quickly energy (stress) accumulates in a fault zone and is used as an important input parameter in seismic hazard assessment (Liu et al., 2021). The slip rate in the study area was calculated based on the age and displacement of each trench. The slip rate was calculated using the MRE and MRE displacement only, and the cumulative slip rate was calculated using the cumulative displacement and the oldest age in the trench section and drilling core. The slip rate calculated using the MRE can be considered maximum because it uses the shortest time for the last earthquake. The cumulative slip rate reflects trends over a relatively longer period than the MRE; therefore, it may show a slip rate closer to the mean but is likely to be an underestimate. The minimum overall slip rate was 0.02 mm/yr, maximum was 0.38 mm/yr, and average was 0.14 mm/yr (Fig. 10). The most reliable slip rate of each trench was 0.04–0.11 mm/yr, which is equal to the slip rate of the MRE obtained for Trench 1, where the second and third of the three earthquakes were identified. The long-time interval and displacement of Trench 3 included the MRE from the AE so it is reasonable to consider the slip rate of Trench 3 to be a cumulative slip rate (Fig. 10). The slip rates from the MRE ranged from 0.20–0.35 mm/yr, suggesting a maximum slip rate that can be derived for the study area. The cumulative slip rates derived for each trench indicate a range of 0.02–0.06 mm/yr. The difference in slip rates can be inferred in two ways. First, slip rates during the Quaternary in the study area averaged 0.02–0.06 mm/yr but may have accelerated in

the recent Holocene due to changes in the surrounding tectonic setting, such as changes in the thickness of the subducting plates and increases or decreases in far-field stress, but also due to local factors such as seasonal climate, fluid inflow, and
515   increased stress accumulation on faults. Second, the discontinuous distribution of Quaternary sediments may have led to an overestimation of the slip rate using the MRE. There are two distinct types of sediments in the trench section: light brown, relatively coarse-grained sediments of mid-to-late Pleistocene age, which were observed to be tilted in the vicinity of the fault, and dark brown, relatively coarse-grained, nearly horizontal Holocene sediments (Table 1, Figs. 3-7). The exact absolute time interval between these two deposits is unknown; however, there was unconformity and the MRE mostly cut Holocene
520   sediments (<10,000 years). The unconformity in deposition is likely to have missed the earthquakes between the two periods and the MRE cut through younger sediments (Sadler effect; Sadler, 1999), causing the maximum slip rate to be overestimated. The recurrence interval in the study area was also estimated. Based on the minimum of three earthquakes estimated from the number of faulting events, the interval between the MRE and PE was 14–72 ka and between the PE and AE was 62–129 ka (Fig. 9). The recurrence interval inversely calculated using the slip rate (RI=event per displacement/slip rate; Wallace, 1970)
525   was approximately 9.5 ka using the slip rate of the MRE (0.21 mm/yr) and the event per displacement (average 2 m) and approximately 23 ka using the long-term slip rate (0.031 mm/yr) and the displacement per event (average 0.7 m) of the PE and AE. Although no clear recurrence interval has been presented in Korean paleoseismological studies, Kim and Lee (2023) used ESR ages to suggest that the Yangsan Fault follows a quasiperiodic model and has a recurrence interval of approximately 100 ka, which is closely related to the interval of interglacial sea-level loading over the Late Quaternary. Determining the
530   recurrence interval and earthquake periodicity model of the intraplate is difficult. Earthquakes occur in a regular pattern along the boundary in an interplate; however, in an intraplate, they often occur randomly, depending on the heterogeneous and complex interior structure (Liu and Stein, 2016). Long recurrence intervals of 400 ka have been reported for intraplate (Williams et al., 2017); therefore, we can make a conservative estimate that the recurrence interval of the study area is over 10,000 years. However, the recurrence interval may be shorter if the complexity of the fault zone is combined with external
535   factors, such as increased seismicity on the Korean Peninsula after the Tohoku Earthquake (Hong et al., 2015; 2018) or changes in slip rates.
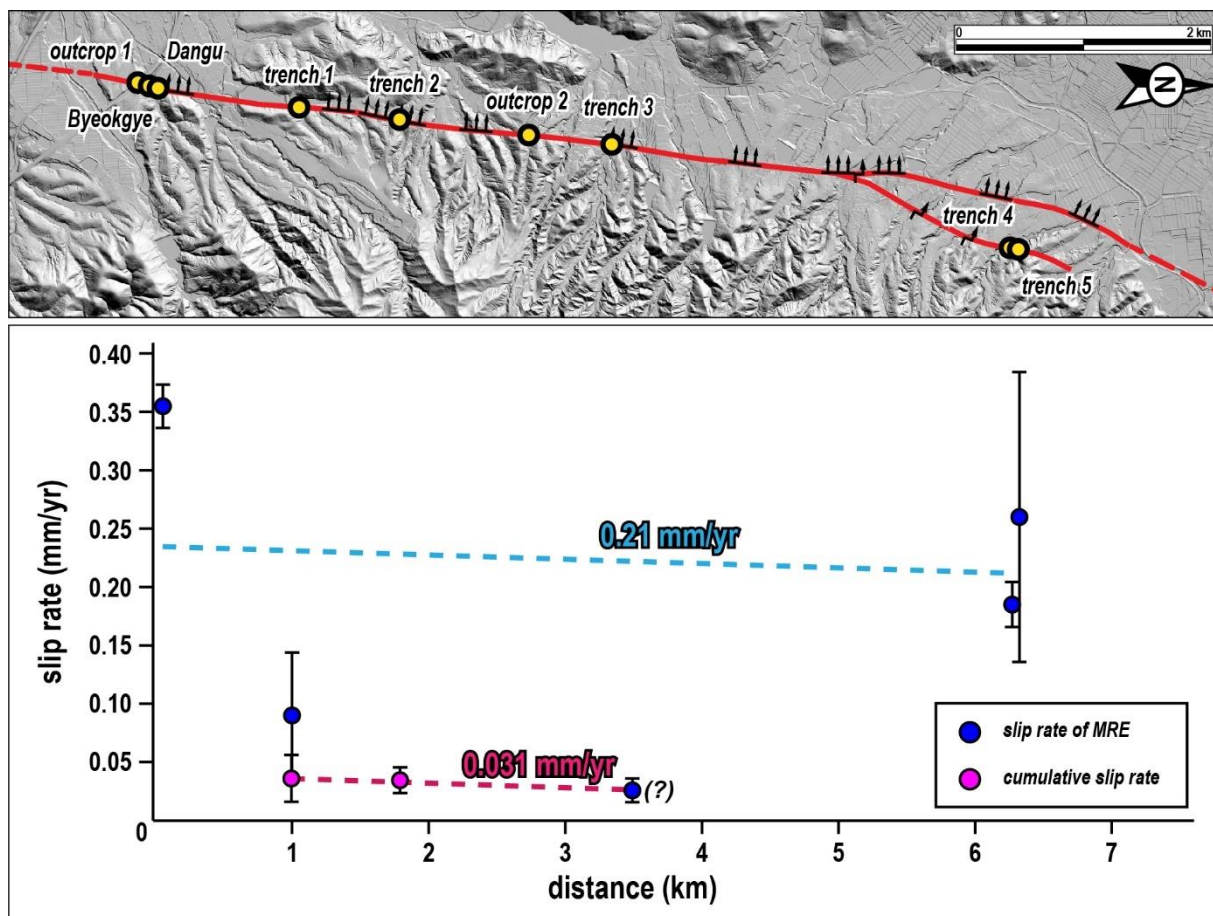
Figure 10: Slip rate graph of the study area. Blue circles indicate slip rate using displacement and age of MRE. Pink circles represent the slip rate using cumulative displacement and age. Dash lines show the trend line and average value of each slip rate. The slip rate in the study area is expected to be between 0.031 and 0.21 mm/yr.

5.2 Structural patterns of Quaternary reactivation of the Yangsan Fault

In all trenches of the study area, the hanging wall of the main fault surface maintained a pre-existing fault core. The exposure of the fault core varied from trench to trench but showed several common features. First, only Holocene sediments were present in the hanging wall of the fault core, with no Middle Pleistocene sediments observed. This indicates that reverse faulting has occurred continuously since at least the Middle Pleistocene. Second, NNE to N-S striking slip surfaces with high-angle dips were present within the fault core, and slickenlines developed on these slip surfaces, indicating dextral strike-slip with rakes of 10° or less. The main fault surface, which cut Quaternary sediments, dictated E-W compression; however, most shear fractures and slip surfaces in the fault core indicated NE-SW compression. Third, the internal structure of the fault core was composed of two or more zones delimited by the slip surface, each showing different types of fault rocks and colors depending on the host rock. Fault rocks of the Cretaceous sedimentary origin were mainly composed of thick, purple-colored fault gouge zones and the captured sandstones were greyish–white lenticular fault breccia or brecciated zones. The Cretaceous volcanic

rocks mainly comprised dark blue–grey fault breccia zones and fault gouges with a thickness of over 10 cm on both sides of the fault breccia zone. Fault rocks of the Cretaceous granite origin were mainly observed as white fault breccia zones characterized by numerous veins and a clayey matrix due to hydrothermal alteration. In the case of alkaline granites, bright
555 orange fault breccia mainly developed, and a 2–3 cm fault gouge was observed surrounding the lenticular fault breccia. The descriptive features of the fault core internal structure and the occurrence of slickenlines and shear surfaces indicative of NE-SW compression within the fault core are similar to the reported fault core features of the Yangsan Fault (Cheon et al., 2017, 2019; Kim et al., 2022). Fieldwork and previous studies revealed that the alkaline granite in the study area is a dextral offset marker of the Yangsan Fault (Hwang et al., 2004, 2007a, b), and vertical cores from the footwall of Trench 2 revealed that the
560 basement rock is alkaline granite. In addition, Kim et al. (2022) conducted inclined corings and microstructural studies in the vicinity of Trench 1 and identified a fault damage zone, undeformed wall rock, and a fault core approximately 25 m wide within the alkaline granite of the footwall. Multiple lines of evidence demonstrate that the pre-existing fault core distributed on the trenches is the main fault core zone of the Yangsan Fault cutting the alkali granite and that the western boundary of the main fault core was reactivated during the Quaternary. The fault slip surface where the alkali granite contacts the main fault
565 core suggests that it was in a more slip-prone state (e.g., Low coefficient of friction; Woo et al., 2015) during the Quaternary than other slip surfaces within the fault core. The NE-SW compression shown by the slip surfaces and shear fractures within the pre-existing fault core is also consistent with a stress field that generates dextral strike-slip movement, which is the major deformation of the Yangsan Fault (Cheon et al., 2017, 2019). Taken together, these results demonstrate that the western boundary of the fault core within the Yangsan fault zone has been reactivated as a dextral strike-slip with a small reverse
570 component since at least the Early Pleistocene, causing surface rupture in the study area.

Given that the present-day ENE-WSW stress field acting on the Korean Peninsula has existed since 5 Ma (Kim et al., 2016), it is reasonable to infer that the study area has been continuously faulted with the same kinematics since the beginning of the Quaternary. The hanging wall of the main fault surface that cuts the Quaternary sediments is composed of a pre-existing fault core not only in the study area but also in other Quaternary fault sites along the Yangsan Fault. In all reported Quaternary fault
575 sites, except for one (Bogyeongsa site) north of the study area, the fault core was distributed in the hanging wall and had a top-to-the west geometry (Kyung, 2003; Ko et al., 2022; Lee et al., 2022; Kim et al., 2023). The top-to-west geometry is also confirmed topographically. Where the Quaternary faults are located north of the study area, the average elevation is higher, and the relief is more mountainous on the east side where the hanging wall is located. In the Bogyeongsa section, which does not have this similarity, the topography is uplifted to the west and is the only Quaternary fault of the Yangsan Fault with a top-
580 to-the east geometry. In the southern part of the study area, the pre-existing fault core constitutes a hanging wall up to Mihori, Ulju-gun (MH, IBN trench in Kim et al., 2023), located in southern Yangsan Fault (Kim et al., 2023). However, the Quaternary fault sites south of Mihori show different deformation patterns from those to the north. In the Inbo trench (IB), which is closest to the IBN trench, fault planes developed between unconsolidated sediments (Cheon et al., 2020a), these features are also present in other fault sites of the southern Yangsan Fault (Choi et al., 2012). The deformation pattern of the Quaternary faulting
585 of the northern Yangsan Fault is top to the west, with the main fault core and unconsolidated sedimentary layers abutting the

main fault surface, while the Quaternary faulting of the southern Yangsan Fault is characterized by the development of the main fault surface between unconsolidated sedimentary layers. The Mihori area, which has been suggested as the boundary between the central and southern Yangsan faults (Choi et al., 2017), is a point location where the trend of the Yangsan Fault changes on the surface. The fault-line valley was relatively wide south of Mihori and narrowed as it passed through the Mihori
590   area. In addition, the distribution of aftershocks was concentrated in this area during the 2016 Gyeongju earthquake and the geometry of surface geological surveys and faults suggests that this area is prone to deformation (Kim et al., 2017). Taken together, the topographic, structural, seismic, and paleoseismic features of the Mihori area suggest a high probability of large earthquakes or future earthquakes.
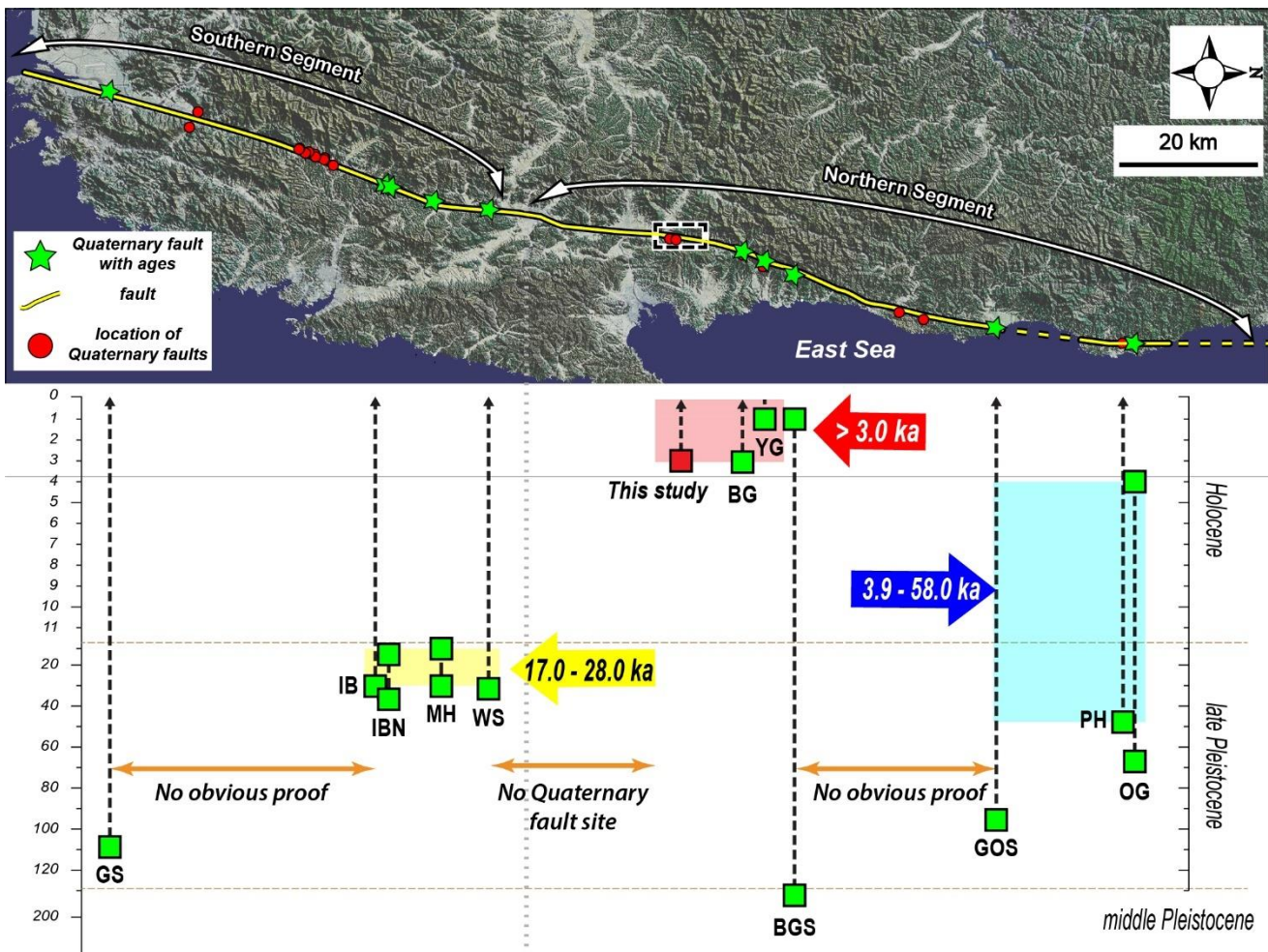
595   **Figure 11: MRE of Yangsan fault. Green stars indicate where MREs have been identified due to the presence of Quaternary sediment ages. GS: Gasan (Lim et al., 2022), IB: Inbo (Cheon et al., 2020a), IBN: Inbonorth, MH: Miho, WS: Wolsan (Kim et al., 2023), BG: Bangok (Lee, 2023), YG: Yugye (Kyung, 2003), BGS: Bogyeongsa (Lee et al., 2022), GOS: Goesi (Ko et al., 2022), PH: Pyoenghae (Choi et al., 2012), OG: Ogok (Han et al., 2021). "No obvious proof" refers to areas where sites that cut unconsolidated sediments are present but not dated.**

5.3 MRE and activity for each segment of the Yangsan Fault

The MRE of the Yangsan Fault was examined section-by-section by synthesizing previous studies (Fig. 11). First, the MREs of the Ogok, Pyeonghae, and Goesi sites in the northernmost region of the northern Yangsan Fault were both Late Pleistocene and Holocene (Choi et al., 2012; Han et al., 2021; Ko et al., 2022). The Yeongdeok area, which extends from the Goesi trench to the northern part of the Bogyeongsa site, has several reported Quaternary fault sites but no clear evidence of Quaternary faulting because they either cut unconsolidated sediments with no age constraint or do not cut unconsolidated sediments and have only ESR ages of the fault gouge (Choi et al., 2012). The Bogyeongsa site is between the Middle Pleistocene and Holocene (154±13–0.9±0.1 ka; Lee et al., 2022) and the MRE of the Yugye site located at the northern Yangsan faults is after Holocene (AD 646), making it the youngest MRE in the entire Yangsan fault (Kyung, 2003). The MRE of the Bangok site, closest to the study area, and the study area both occurred after the Holocene (Lee, 2023). The Angang area beyond the study area has no reports of Quaternary faulting and at the Wolsan site, in the northernmost part of the southern Yangsan Fault, the MRE is Late Pleistocene. The Miho, Inbonorth, and Inbo sites of the southern Yangsan Fault are all Late Pleistocene and the southernmost part of the Yangsan Fault, the Gasan site, is after the Late Pleistocene (Lim et al., 2021). Looking at the MRE trends by area, the northern part of the Bogyeongsa site experienced MREs after the Late Pleistocene, the section between Yugye and Byeokgye experienced surface rupture in the Holocene, and the southern Yangsan fault from the Wolsan site to the Gasan site experienced MREs mostly in the Late Pliocene. At first glance, it may appear that the section between Yugye and the study area was more active with Holocene MREs but the timing of the MREs alone was inadequate to assess which zone was more active. For example, Holocene surface rupture may indicate that the fault has a short recurrence interval; conversely, a fault with an older MRE may have a higher potential for future earthquakes because recent faulting events may have released stress accumulation. Deviation in the timing of MREs at different sites or sections can be a direct indication of the fault motion that caused the surface rupture; however, uncertainty in age constraints due to the presence or absence of sediments must be considered. The MRE is an important factor in activity assessment because if it has a recurrence interval, the elapsed time can be calculated, which can be used to predict future earthquakes. However, the activity considered using MRE alone can be misleading; therefore, it is necessary to derive recurrence intervals and elapsed time to accurately predict earthquakes based on paleoseismic data. Ultimately, activity assessment should consider not only paleoseismic data but also topographic, structural, seismic, and geodetic aspects.

6 Conclusion

We conducted surface geological surveys, trenching, coring, OSL/IRSL dating, radiocarbon dating, ESR dating, and cosmogenic nuclides dating along the lineament extracted from topographic analysis using high-resolution LiDAR imagery at the Yangsan Fault. The primary aim was to identify the surface ruptures that occurred during the Quaternary period, derive structural features, and gather paleoseismic data for the Quaternary fault. The main conclusions are as follows:

(1) A comprehensive analysis, combining two previously reported Quaternary fault sites (Byeokgye and Dangu), two newly discovered natural outcrop sites, five trenches, coring surveys, and dating of unconsolidated sediments, charcoal, and fault rocks, revealed a 7.6 km Quaternary surface rupture along the Yangsan Fault. (2) The Quaternary faults in the study area exhibited an east-dipping geometry with an N-S to NNE strike and moved as a dextral strike-slip with a reverse slip component during the Quaternary. (3) At least three faulting events were interpreted from the trench sections, with an MRE of approximately 3,000 years ago. The MRE displacement ranged from 0.64 to 3.29 m, cumulative displacement from 3.1 to 94 m, displacement per event before the MRE from 0.33 to 1.1 m, and maximum magnitude using the MD from M_w 6.7–7.2. The slip rate was 0.03–0.21 mm/yr, with a recurrence interval of at least 10,000 years. (4) The Quaternary structural features indicate that during the Quaternary period, the western boundary of the main fault core of the Yangsan Fault was reactivated under ENE-WSW compressional stress. The top-to-west geometry is consistent with that observed throughout the Yangsan Fault. (5) The southern part of the northern Yangsan Fault, including the study area, documents a Holocene MRE that is younger than those documented in the southern Yangsan Faults.

Surface rupturing has been observed along most sections of the Yangsan fault and in the study area, and basic paleoseismic studies continue to be reported (Fig. 11; Lee et al., 2022; Kim et al., 2023). The challenge is that Korea's geologic diversity results in a large number of faults that need to be studied (e.g., Chugaryeong Fault). Only then will it be possible to properly understand the seismicity pattern of Korea and the earthquakes in the low active intraplate regions. Although the study results are only for a small 10 km section of the Yangsan fault with a 200 km extension, the San Andreas fault, which has high-resolution paleoseismic data from more than 200 trenches, also started out in the same way. In particular, studying seismic hazards on the Korean Peninsula, with its urbanization, cultivated land, slow slip rates, long recurrence intervals, and fast erosion rates, is a challenge. This research will hopefully contribute to the research on earthquake hazards in Korea, which is just beginning to advance. Furthermore, this study contributes valuable insights for seismic hazard assessment in the region and offers a broader understanding of intraplate earthquake dynamics, thereby aiding earthquake prediction efforts.

Appendices

655 Appendix A. Calculation of true displacement

The true displacement (S_t) can be calculated using a trigonometric function that considers the vertical displacement (S_v), fault dip angle (α), rake (γ), and their relationships (Fig. A1; Eq. A1). Assume that the attitude of the marker in the cross-section at each trench is nearly horizontal in three dimensions and the angle (β) of the cross-section is nearly vertical, then the two factors are perfectly horizontal and vertical, respectively. Thus, the vertical separation (S_{vm}) and vertical displacement (S_v) measured

660 in the cross-section are equal.

Therefore,

$$S_{vm} = S_v, S_m = \frac{S_v}{\sin \alpha}, S_t = \frac{S_m}{\sin \gamma} \quad \text{(A1)}$$

We calculate true displacement (S_t) using Eq. (A1) for vertical separation (S_{vm}) of the marker measured in the trench section, as shown in Table 6.
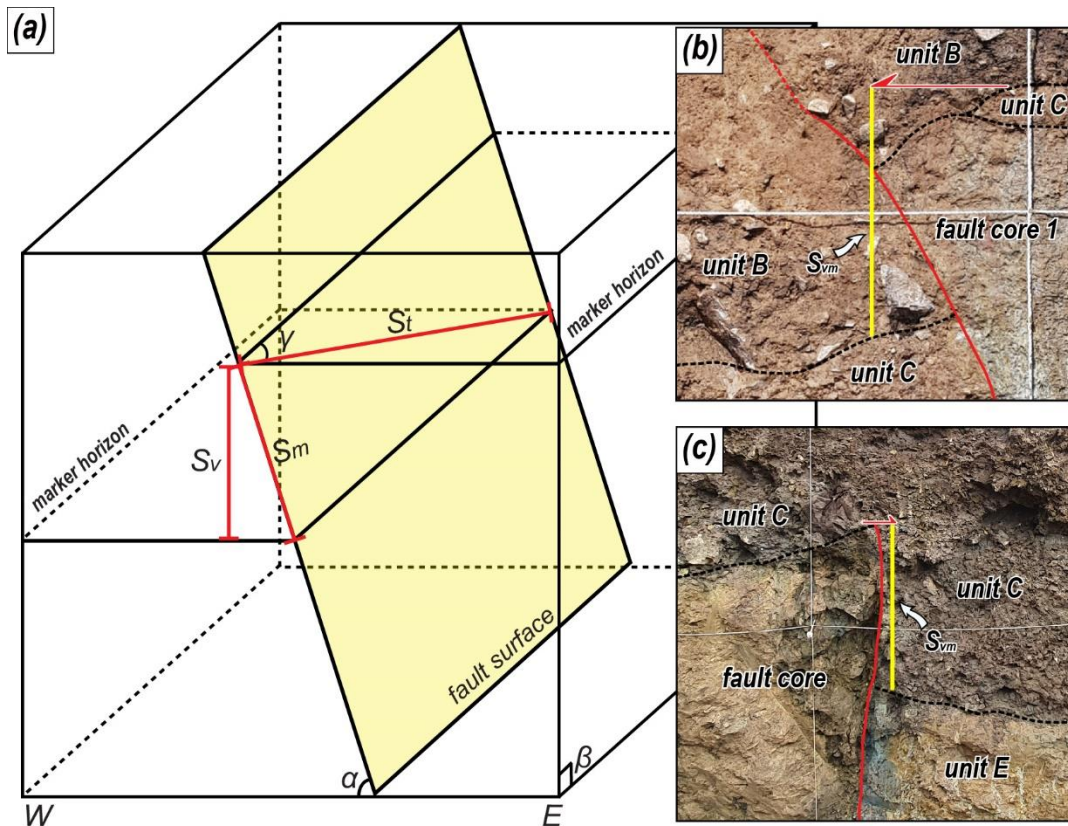
665

Figure A1: (a) Schematic diagram showing how to calculate true displacement. S_t: true displacement, S_v: vertical displacement, S_m: dip separation, α: dip of fault surface, β: dip of cut slope, γ: rake of the striation (modified from Xu et al., 2009). (b and c) Photographs showing the measured vertical separation of the trenches 1 and 5. S_{vm}: vertical separation.

670   Appendix B. Description of the Outcrop 1 and 2

Outcrop 1 is located 30 m south of the Byeokgye site (Fig. 2c). A high-angle fault cut the Cretaceous volcanic rocks and unconsolidated sediments interbedded with gravel deposits and sand layers (Fig. B1a). The fault trace was partially recognized on the surface based on the lithological distribution. The fault core consisted of a 20 cm-wide fault breccia with a fault surface attitude of N12°E/84°NW, and no clear slickening was observed (Fig. B1b). Outcrop 2, on the extension of the main lineament,

675   is located 2.7 km north of the Byeokgye site (Fig. 2c). The outcrop contained highly weathered purple sedimentary rock overlying unconsolidated sediments (Fig. B1c). The NNE-striking fault surface dipped toward the east with a low angle. The purple sedimentary rock of the hanging wall was mostly clayey and may be either a pre-existing purple fault gouge or weathered purple Cretaceous sedimentary rock. The fault core adjacent to the unconsolidated deposits consisted of a 2–3 cm thick foliated fault gouge (Fig. B1d). The foliation is subparallel to the slip surface. The unconsolidated gravel deposits have

680   poor sorting, and angular clasts consist of sandstone, granitic, and volcanic rocks. No clear slickenlines were observed, owing to highly weathered outcrop conditions. We could not date either outcrop because the clast-rich sediments were not suitable for OSL dating and did not include organic material for ^{14}C dating.
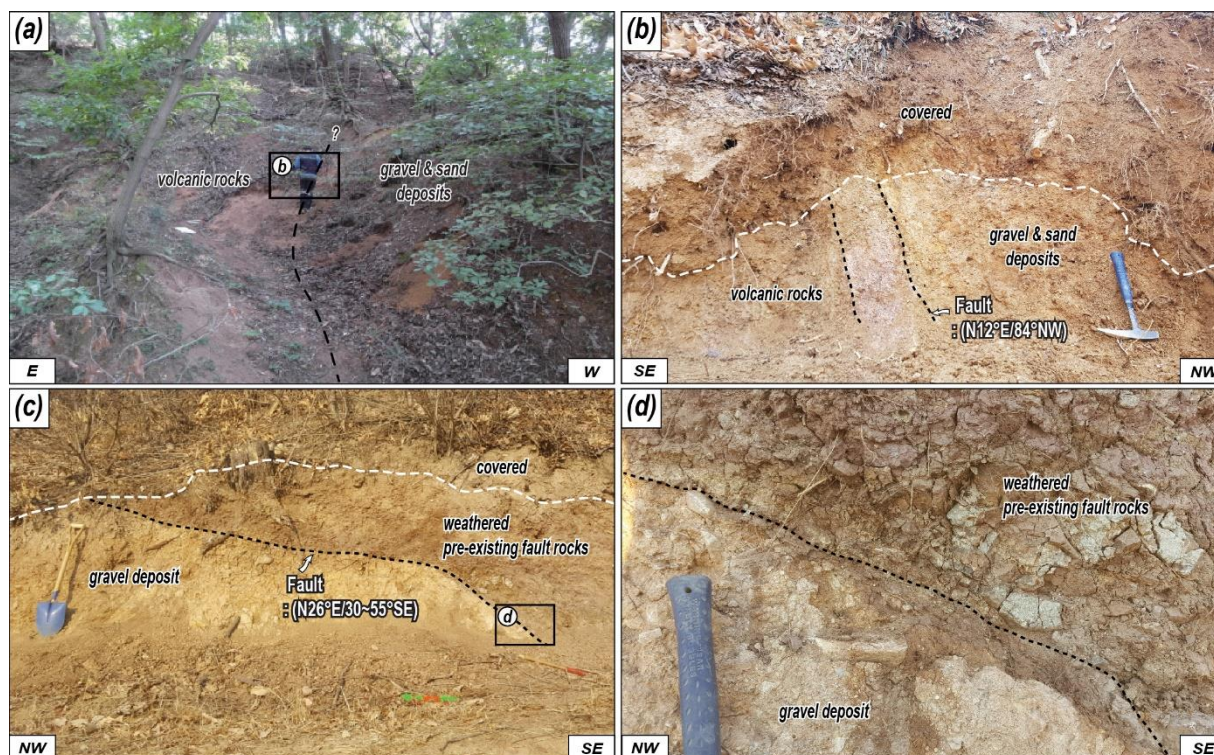
Figure B1: Photographs showing the outcrops of the fault which that cut the unconsolidated sediments. (a) Fault trace on the surface.
685   **(b) NNE striking fault cut the boundary between volcanic rocks and gravel and sand deposits. The fault rock is composed of breccia.**
(c) Weathered pre-existing fault rocks thrust gravel deposits along the low-angle fault surface. (d) Close-up photograph of the fault
surface. A 2-3 cm thick fault gouge forms a boundary between two different rocks.

Appendix C. Coring at the Trench 2

690   We cored the footwall of Trench 2. Unconsolidated sand and gravel deposits alternated up to 24 m below the surface. From 24 m to 32.8 m, the material consisted of a granite wash, at the base of which a 1.2 m thick weathering zone was recognized. From 34 m onwards, the bedrock is clearly identified as alkaline granite (Fig. C1). We performed ^{10}Be-^{26}Al isochron burial dating on the granite wash immediately above the basement rock.

695   **Figure C1: Photograph showing drilled core. The lowermost of the unconsolidated sediments, the granite wash, directly overlies bedrock. Cosmogenic ^{10}Be-^{26}Al isochron dating samples were taken from this granite wash.**

Appendix D. Detailed OSL, IRSL, and ^{10}Be-^{26}Al isochron burial age dating results

700   The graphs of the detailed results of 1-2 representative samples per trench for OSL and IRSL. We selected samples from sediments cut into the MRE and from sediments overlying the MRE. The graphs include decay curves, probability density graphs, and ^{10}Be-^{26}Al isochron graphs. The tables also include dose rates, equivalent doses and luminescence ages of the samples from each trench.
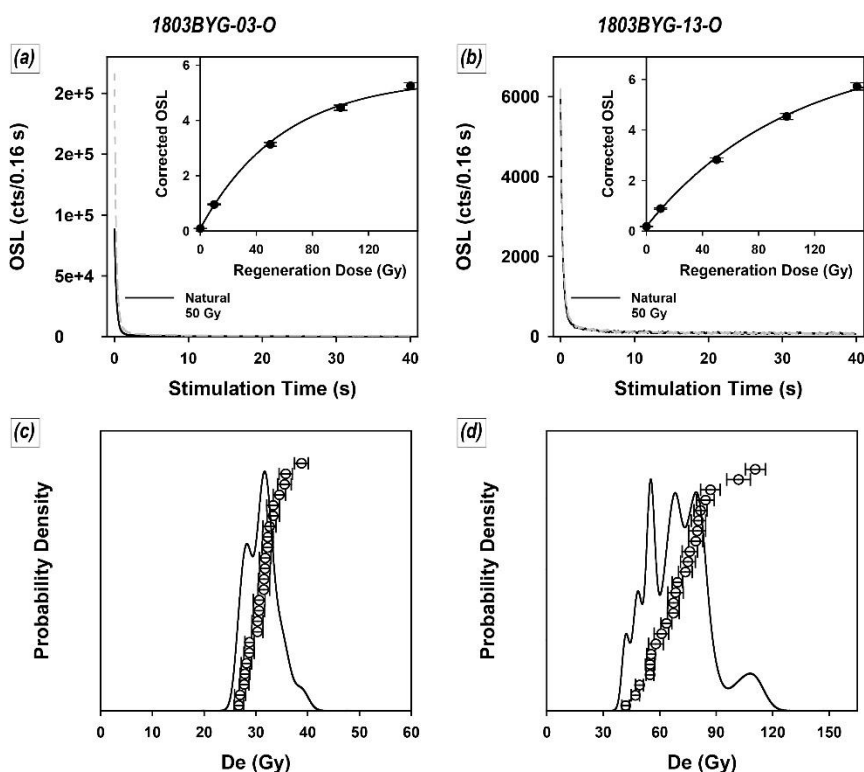
Figure D1: Representative quartz OSL decay curves (a, b) and probability density graph (c, d) of Trench 1.

705
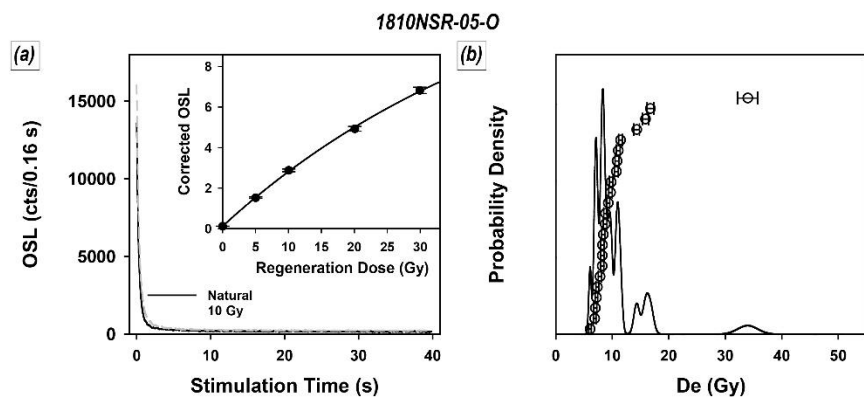
Figure D2: Representative quartz OSL decay curves (a, b) and probability density graph (c, d) of Trench 2.
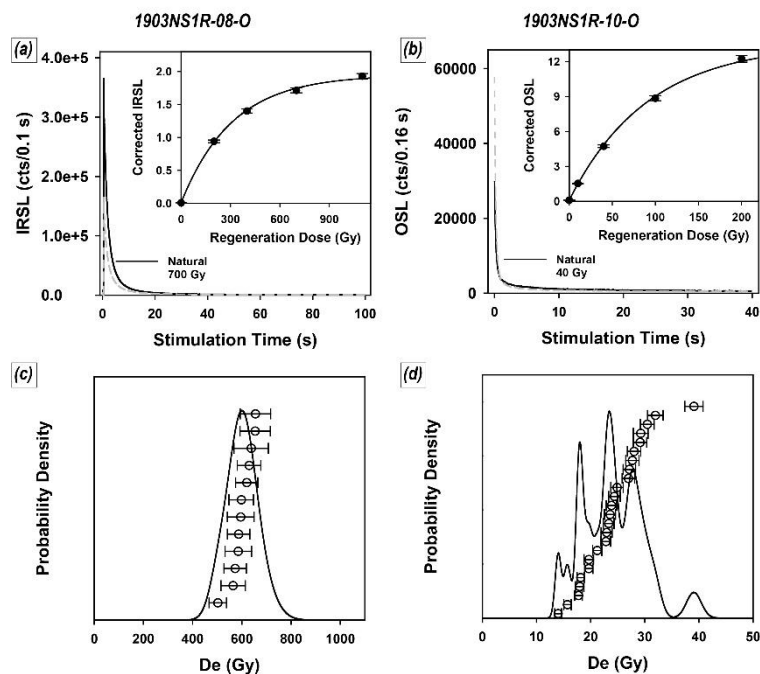
Figure D3: Representative quartz OSL/IRSL decay curves (a, b) and probability density graph (c, d) of Trench 3.

710
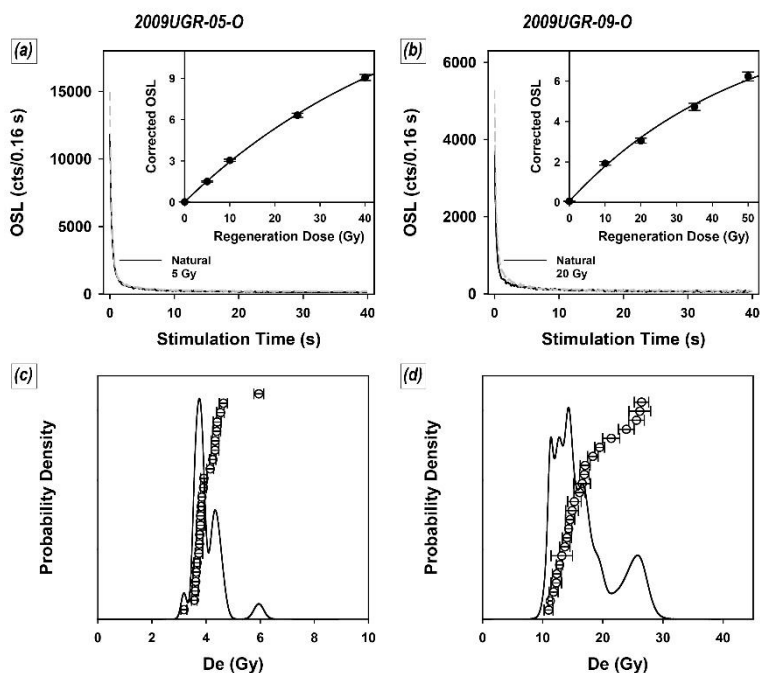
Figure D4: Representative quartz OSL decay curves (a, b) and probability density graph (c, d) of Trench 4.
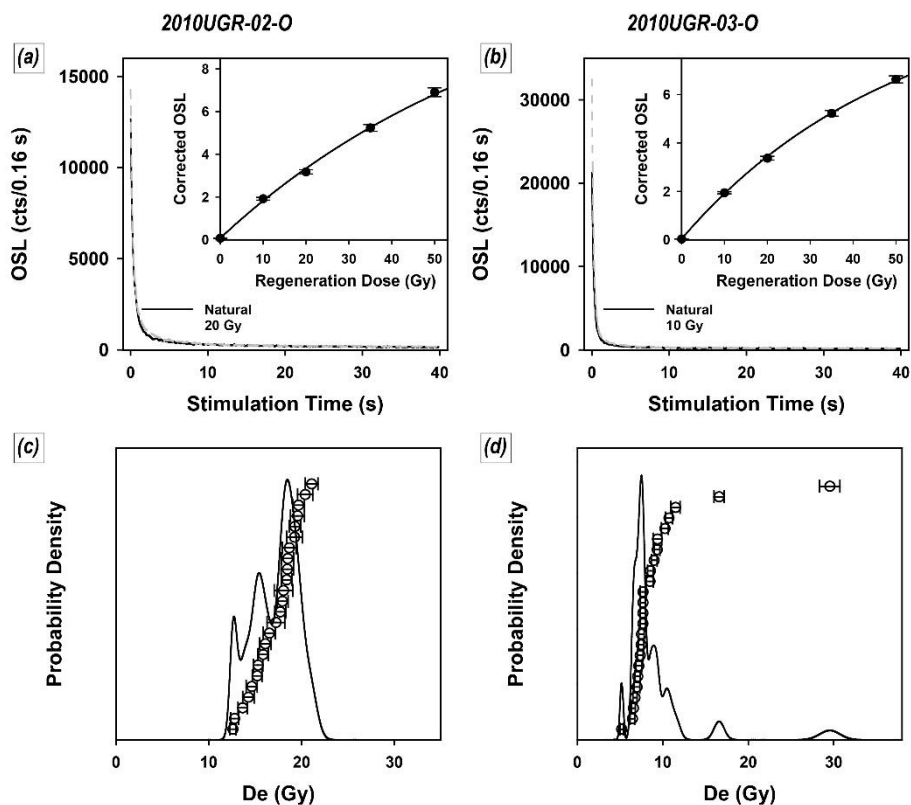
Figure D5: Representative quartz OSL decay curves (a, b) and probability density graph (c, d) of Trench 5.

715
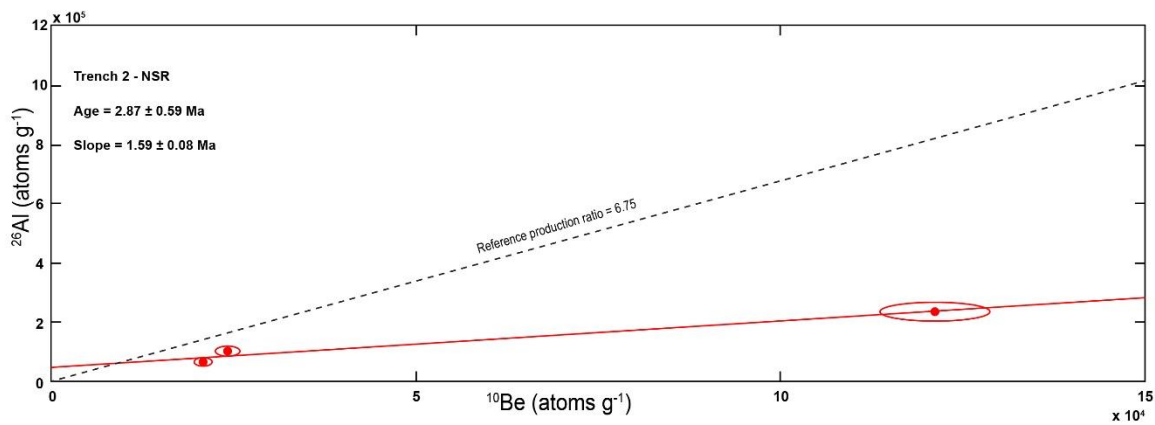
Figure D6: ^{10}Be-^{26}Al isochron graph of coring samples in Trench 2.

Table D1: Dose rates, equivalent doses and luminescence ages of the samples from the Trench 1

Method	Sample code	Dose rate[a] (Gy/ka)	Water content[b] (%)	Equivalent dose (Gy)	Fading rate (g_{2days}, %/dec.)	Aliquots used (n)	age[c] (ka, 1σ SE)
	1803BYG-01-O	3.26 ± 0.08	13	4.2 ± 0.2	-	24	1.3 ± 0.1
	1803BYG-02-O	3.54 ± 0.09	16	33 ± 1	-	24	9 ± 1
	1803BYG-03-O	3.00 ± 0.08	17	31 ± 1	-	24	10 ± 1
Quartz OSL	1803BYG-05-O	3.16 ± 0.08	14	16 ± 1	-	24	4.9 ± 0.3
	1803BYG-06-O	3.37 ± 0.09	12	11 ± 1	-	24	3.2 ± 0.2
	1803BYG-13-O	4.02 ± 0.11	13	68 ± 4	-	24	17 ± 1
	1803BYG-14-O	3.31 ± 0.09	10	27 ± 1	-	24	8.1 ± 0.3
	1803BYG-04-O	3.90 ± 0.09	18	537 ± 23	0.8 ± 0.3	12	146 ± 8
	1803BYG-07-O	4.36 ± 0.10	16	733 ± 31	0.7 ± 0.2	12	177 ± 7
K-feldspar pIRIR$_{225}$	1803BYG-08-O	3.99 ± 0.09	18	558 ± 18	1.1 ± 0.3	24	151 ± 8
	1803BYG-09-O	4.21 ± 0.10	22	561 ± 21	1.0 ± 0.3	12	143 ± 7
	1803BYG-10-O	3.95 ± 0.10	20	581 ± 20	1.5 ± 0.3	12	164 ± 8
	1803BYG-11-O	4.12 ± 0.09	18	594 ± 19	1.0 ± 0.4	12	155 ± 8
	1803BYG-12-O	4.63 ± 0.11	15	613 ± 21	1.0 ± 0.3	12	142 ± 7

720 **[a] Wet total dose rates. The activities of each radionuclide were converted to dose rates using the data presented by Liritzis et al. (2013). Cosmic ray dose rates were estimated using the method suggested by Prescott and Hutton (1994). The internal dose rate of K-feldspar was calculated assuming internal K content of 12.5 % and by using the methods proposed by Mejdahl (1987) and Readhead (2002). For deriving the total dose rates absorbed by K-feldspar, the internal dose rate of 0.736±0.04 Gy/ka was added to the external ones of each sample.**

725 **[b] Present water content.**

[c] Fading-corrected ages in the case of K-feldspar

Table D2: Dose rates, equivalent doses and luminescence ages of the samples from the Trench 2

Method	Sample code	Dose rate[a] (Gy/ka)	Water content[b] (%)	Equivalent dose (Gy)	Aliquots used (n)	age[c] (ka, 1σ SE)
Quartz OSL	1810NSR-05-O	3.09 ± 0.08	18	9.9 ± 0.8	23	3.2 ± 0.3
	1810NSR-06-O	3.46 ± 0.09	14	12 ± 1	22	3.4 ± 0.4
	1810NSR-07-O	2.55 ± 0.06	19	47 ± 2	24	19 ± 1

[a] **Wet total dose rates. The activities of each radionuclide were converted to dose rates using the data presented by Liritzis et al.**
730 **(2013). Cosmic ray dose rates were estimated using the method suggested by Prescott and Hutton (1994).**

[b] **Present water content.**

Table D3: Dose rates, equivalent doses and luminescence ages of the samples from the Trench 3

Method	Sample code	Dose rate[a] (Gy/ka)	Water content[b] (%)	Equivalent dose (Gy)	Fading rate (g$_{2days}$, %/dec.)	Aliquots used (n)	age[c] (ka, 1σ SE)
Quartz OSL	1903NS1R-10-O	3.67 ± 0.09	23	23 ± 1	-	24	6.4 ± 0.4
K-feldspar pIRIR$_{225}$	1903NS1R-02-O	4.01 ± 0.09	18	606 ± 22	1.8 ± 0.6	12	173 ± 11
	1903NS1R-03-O	4.11 ± 0.09	16	600 ± 16	2.4 ± 0.4	12	175 ± 9
	1903NS1R-08-O	4.55 ± 0.10	15	595 ± 18	0.6 ± 0.3	12	137 ± 6

[a] **Wet total dose rates. The activities of each radionuclide were converted to dose rates using the data presented by Liritzis et al.**
735 **(2013). Cosmic ray dose rates were estimated using the method suggested by Prescott and Hutton (1994). The internal dose rate of K-feldspar was calculated assuming internal K content of 12.5 % and by using the methods proposed by Mejdahl (1987) and Readhead (2002). For deriving the total dose rates absorbed by K-feldspar, the internal dose rate of 0.736±0.04 Gy/ka was added to the external ones of each sample.**

[b] **Present water content.**

740 [c] **Fading-corrected ages in the case of K-feldspar**

Table D4: Dose rates, equivalent doses and luminescence ages of the samples from the Trench 4

Method	Sample code	Dose rate[a] (Gy/ka)	Water content[b] (%)	Equivalent dose (Gy)	Aliquots used (n)	age[c] (ka, 1σ SE)
	2009UGR-05-O	3.11 ± 0.08	12	3.9 ± 0.1	24	1.3 ± 0.1
	2009UGR-06-O	2.97 ± 0.08	11	3.6 ± 0.1	24	1.2 ± 0.1
Quartz OSL	2009UGR-07-O	3.44 ± 0.09	12	0.5 ± 0.1	24	0.15 ± 0.03
	2009UGR-08-O	3.41 ± 0.09	13	0.5 ± 0.1	24	0.15 ± 0.03
	2009UGR-09-O	2.75 ± 0.07	12	16.1 ± 0.9	24	5.9 ± 0.4

[a] Wet total dose rates. The activities of each radionuclide were converted to dose rates using the data presented by Liritzis et al.
745 **(2013). Cosmic ray dose rates were estimated using the method suggested by Prescott and Hutton (1994).**

[b] Present water content.

Table D5: Dose rates, equivalent doses and luminescence ages of the samples from the Trench 5

Method	Sample code	Dose rate[a] (Gy/ka)	Water content[b] (%)	Equivalent dose (Gy)	Aliquots used (n)	age[c] (ka, 1σ SE)
	2010UGR-01-O	3.19 ± 0.08	14	32 ± 3	23	10 ± 1
Quartz OSL	2010UGR-02-O	3.47 ± 0.09	14	17 ±1	24	4.8 ± 0.2
	2010UGR-03-O	2.77 ± 0.07	21	7.9 ± 0.3	24	2.8 ± 0.1
	2010UGR-04-O	2.96 ± 0.07	17	7.6 ± 0.2	24	2.6 ± 0.1

[a] Wet total dose rates. The activities of each radionuclide were converted to dose rates using the data presented by Liritzis et al.
750 **(2013). Cosmic ray dose rates were estimated using the method suggested by Prescott and Hutton (1994).**

[b] Present water content.

Data availability. All detailed age dating data are available in Tables 2-5, D1-D5. Questions or requests for original photomosaic of trenches can be sent to the corresponding author.

755 **Author contributions.** Conceptualization: SH, HCK, Funding acquisition: SM, Investigation: SM, HCK, SL, YBS, JHC, SJK, Project administration: SM, Supervision: SM, Validation: YBS, JGC, SJK, Visualization: SM, SJK, Writing – original draft preparation: SH, Writing – review & editing: SH, YBS, JHC, SM,

Competing interests. The authors declare that they have no conflicts of interest.

760

Financial support.

This research was supported by a grant (2022-MOIS62-001(RS-2022-ND640011)) of National Disaster Risk Analysis and Management Technology in Earthquake funded by Ministry of Interior and Safety (MOIS, Korea).

765 **References**

Ansari, K. and Bae, T.S.: Contemporary deformation and strain analysis in South Korea based on long-term (2000–2018) GNSS measurements, Int. J. Earth Sci. (Geol. Rundsch.), 109, 391–405, https://doi-org-ssl.oca.korea.ac.kr/10.1007/s00531-019-01809-4, 2020.

Argus, D.F., Gordon, R.G., Heflin, M.B., Ma, C., Eanes, R.J., Willis, P., Peltier, W.R., and Owen, S.E.: The angular velocities
770 of the plates and the velocity of the Earth's centre from space geodesy, Geophys. J. Int., 18, 1-48, https://doi:10.1111/j.1365-246X.2009.04463.x, 2010.

Ashurkov, S.V., San'kov, V.A., Miroschnichenko, A.I., Lukhnev, A.V., Sorokin, A.P., Serov, M.A., and Byzov, L.M.: GPS geodetic constrains on the kinematics of the Amurian Plate, Russ. Geol. Geophys., 52, 239-249, https://doi.org/10.1016/j.rgg.2010.12.0172, 2011.

775 Atkinson, G.M., Finn, W.D.L. and Charlwood, R.G.: Simple computation of liquefaction probability for seismic hazard applications, Earthq. Spectra, 1, 107-123, https://doi.org/10.1193/1.1585259, 1984.

Balco, G., and Rovey, C.W.: An isochron method for cosmogenic-nuclide dating of buried soils and sediments. Am. J. Sci., 308, 1083–1114, https://doi.org/10.2475/1 0.2008.02, 2008.

Bird, P.: An updated digital model of plate boundaries, Geochem. Geophy. Geosy., 4,
780 1027, https://doi.org/10.1029/2001GC000252, 2003.

Bonilla, M. G., Mark, R. K., and Lienkaemper, J. J.: Statistical relations among earthquake magnitude, surface rupture length, and surface fault displacement, B. Seismol. Soc. Am., 74, 2379–2411, https://doi.org/10.1785/BSSA0740062379,1984.

Bronk Ramsey, C.: Methods for summarizing radiocarbon datasets, Radiocarbon, 59, 1809-1833, https://doi.org/10.1017/RDC.2017.108, 2017.

785 Buylaert, J.P., Jain, M., Murray, A.S., Thomsen, K.J., Thiel, C., and Sohbati, R.: A robust feldspar luminescence dating method for Middle and Late Pleistocene sediments, Boreas, 41, 435–451, https://doi.org/10.1111/j.1502-3885.2012.00248.x, 2012.

Buylaert, J.P., Murray, A.S., Thomsen, K.J., and Jain, M.: Testing the potential of an elevated temperature IRSL signal from K-feldspar, Radiat. Meas., 44, 560–565, https://doi.org/10.1016/j.radmeas.2009.02.007, 2009.

Calais, E., Dong, L., Wang, M., Shen, Z., and Vergnolle, M.: Continental deformation in Asia from a combined GPS solution,
790 Geophys. Res. Lett., 33, L24319, https://doi.org/ 10.1029/2006GL028433, 2006.

Chang, C.-J., and Chang, T.W.: Movement History of the Yangsan Fault based on Paleostress Analysis, J. Eng. Geo., 8, 35-49, 1998.

Chang, C.-J.: Structural characteristics and evolution of the Yangsan fault, SE Korea, Ph.D. thesis, Kyungpook National University, Korea, 2002.

795 Chang, K.H., Woo, B.G., Lee, J.H., Park, S.O., and Yao, A.: Cretaceous and early Cenozoic stratigraphy and history of eastern Kyongsang Basin, S. Korea, J. Geol. Soc. Korea, 26, 471-487, 1990.

Cheon, Y., Cho, H., Ha., S., Kang, H.-C., Kim, J.-S., and Son, M.: Tectonically controlled multiple stages of deformation along the Yangsan Fault Zone, SE Korea, since Late Cretaceous, J. Asian Earth Sci., 170, 188-207, https://doi.org/10.1016/j.jseaes.2018.11.003, 2019.

800 Cheon, Y., Choi, J.-H., Choi, Y., Bae, H., Han, K.-H., Son, M., Choi, S.-J., and Ryoo, C.-R.: Understanding the distribution and internal structure of the main core of the Yangsan Fault Zone: Current trends and future work, J. Geol. Soc. Korea, 56, 61-640, https://doi.org//10.14770/jgsk.2020.56.5.619, 2020a.

Cheon, Y., Choi, J.-H., Kim, N., Lee, H., Choi, I., Bae, H., Rockwell, T.K., Lee, S.R., Ryoo, C.-R., and Choi, H.: Late Quaternary transpressional earthquakes on a long-lived intraplate fault: A case study of the Southern Yangsan Fault, SE Korea,

805 Quatern. Int., 553, 132-143, https://doi.org/10.1016/j.quaint.2020.07.025, 2020b.

Cheon, Y., Ha, S., Lee, S., Cho, H, and Son, M.: Deformation features and history of the Yangsan Fault Zone in the Eonyang-Gyeongju area, SE Korea, J. Geol. Soc. Korea, 53, 95-114, http://doi.org/10.14770/jgsk.2017.53.1.95, 2017.

Choi, J.-H., Kim, Y.-S., and Klinger, Y.: Recent progress in studies on the characteristics of surface rupture associated with large earthquakes, J. Geol. Soc. Korea, 53, 129-157, https://doi.org/10.14770/jgsk.2017.53.1.129, 2017.

810 Choi, J.-H., Yang, S.-J., and Kim, Y.-S.: Fault zone classification and structural characteristics of the southern Yangsan fault in the Sangcheon-ri area, SE Korea, J. Geol. Soc. Korea, 45, 9-28, 2009.

Choi, S.-J., Ghim, Y.S., Cheon, Y., and Ko, K.: The First Discovery of Quaternary Fault in the Western Part of the South Yangsan Fault-Sinwoo Site, Econ. Environ. Geol., 52, 251-258, http://doi.org/10.9719/EEG.2019.52.3.251, 2019.

Choi, S.-J., Jeon, J.S., Song, G.Y., Kim, H.C., Kim, Y.H., Choi, B.Y., Chwae, W.C., Han, J.G., Ryoo, C.-R., Sun, C.-G., Jun,

815 M.-S., Kim, G.-Y., Kim, Y. B., Lee, H. J., Shin, J. S., Lee, Y. S., and Kee, W.-S.: Active fault map and seismic hazard map, National Emergency Management Agency, Seoul, Seoul, 939 pp., 2012.

Crampin, S. and Gao, Y.: Earthquakes can be stress-forecast, Geophy. J. Int., 180, 1124-1127, https://doi.org/10.1111/j.1365-246X.2009.04475.x, 2010.

Delvaux, D., and Sperner, B.: New aspects of tectonic stress inversion with reference to the TENSOR program, in: New

820 Insights into Structural Interpretation and Modelling, edited by Nieuwland, D. A., Geol. Soc., London Spec. Publ., 212, 75-100, https://doi.org/10.1144/GSL.SP.2003.212.01.06, 2003.

Delvaux, D., Moeys, R., Stapel, G., Petit, C., Levi, K., Miroshnichenko, A., Ruzhich, V., and San'kov, V.: Paleostress reconstructions and geodynamics of the Baikal region, Central Asia, Part 2. Cenozoic rifting, Tectonophysics, 282, 1-38, https://doi.org/10.1016/S0040-1951(97)00210-2, 1997.

825 DeMets, C., Gordon, R.G., Argus, D.F., and Stein, S.: Current plate motions, Geophys. J. Int., 101, 425-478, https://doi.org/10.1111/j.1365-246X.1990.tb06579.x, 1990.

DeMets, C., Gordon, R.G., Argus, D.F., and Stein, S.: Effect of recent revisions to the geomagnetic reversal time scale on estimates of current plate motions, Geophys. Res. Lett., 21, 191-2,194, https://doi.org/10.1029/94GL02118, 1994.

England, P., and Jackson, J.: Uncharted seismic risk, Nat. Geosci., 4, 348–349, https://doi.org/10.1038/ngeo1168, 2011.

830 Erlanger, E.D., Granger, D.E., and Gibbon, R.J.: Rock uplift rates in South Africa from isochron burial dating of fluvial and marine terraces, Geology, 40, 1019–1022. https://doi.org/10.1130/G33172.1., 2012.

Geller, R. J., Jackson, D. D., Kagan, Y. Y., and Mulargia, F.: Earthquakes Cannot Be Predicted, Science, 275, 1616-1616, https://doi.org/10.1126/science.275.5306.1616, 1997.

Granger, D. E.: A review of burial dating methods using [26]Al and [10]Be, in: In Situ-Produced Cosmogenic Nuclides and
835 Quantification of Geological Processes: Geological Society of America Special Paper 415, edited by: Siame, L. L., Bourlès, D. L., and Brown, 1–16, https://doi.org/10.1130/2006.2415(01), 2006.

Granger, D.E., and Muzikar, P.F.: Dating sediment burial with in situ-produced cosmogenic nuclides: Theory, techniques, and limitations, Earth Planet. Sc. Lett., 188, 269-281, https://doi.org/10.1016/S0012-821X(01)00309-0, 2001.

Gurpinar, A.: The importance of paleoseismology in seismic hazard studies for critical facilities, Tectonophysics, 408, 23-28,
840 https://doi.org/10.1016/j.tecto.2005.05.042, 2005.

Gwon, O., Park, K., Naik, S. P., Shin, H.-C., and Kim, Y. -S.: A study on the characteristics of fault activity in the southern part of the Ulsan fault using paleoseismic method, J. Geol. Soc. Korea, 57, 109-121, https://doi,org/10.14770/jgsk.2021.57.2.109, 2021.

Gwon, S., Cho, S., Park, D., Choi, W.-H., Nakao, R., Tanaka, T., and Inoue, D.: Microscopic analysis of fault rock using X-
845 ray computed tomography from the Wolsan trench in the middle part of Yangsan fault, SE Korea, J. Geol. Soc. Korea, 56, 273-284, https://doi.org/10.14770/jgsk.2020.56.2.273, 2020.

Ha, S., Son, M., and Seong, Y.B.: Active Fault Trace Identification Using a LiDAR High-Resolution DEM: A Case Study of the Central Yangsan Fault, Korea, Remote Sens., 14, 4838, https://doi.org/10.3390/rs14194838, 2022.

Han, J.-W., Lee, S., Ha, S., Lee, C. H., Seong, Y. B., Kang, H.-C., Kim, M.-C., Gil, T., and Son, M.: A preliminary study on
850 the Quaternary faulting along the northern part of Yangsan Fault and Yeongdeok Fault, in: 76th Annual Meeting of the Geological Society of Korea and 2021 Fall Joint Conference of the Geological Sciences, Jeju, Korea, 26-28 October 2021, 317, 2021.

Han, M., Kim, K.-H., Son, M., Kang, S.Y., and Park, J.-H.: Location of recent micro earthquakes in the Gyeongju area, Geophysics Geophys. Explor., 19, 97-104, https://doi.org/10.7582/GGE.2016.19.2.097, 2016.

855 Hansen, V., Murray, A., Buylaert, J.-P., Yeo, E.Y., and Thomsen, K.: A new irradiated quartz for beta source calibration, *Radiat. Meas., 81, 123*–127, https://doi.org/10.1016/j.radmeas.2015.02.017, 2015.

Heki, K., Miyazaki, S., Takahashi, H., Kasahara, M., Kimata, F., Miura, S., Vasilenko, N.F., Ivashchenko, A., and An, K.-D.: The Amurian Plate motion and current plate kinematics in eastern Asia, J. Geophys. Res., 104, 29, 147-29, 155, https://doi.org/10.1029/1999JB900295, 1999.

860 Hong, T. K., Lee, J., and Houng, S. E.: Long-term evolution of intraplate seismicity in stress shadows after a megathrust, Phys. Earth Planet. In., 245, 59–70, https://doi. org/10.1016/j.pepi.2015.05.009, 2015.

Hong, T. K., Lee, J., Park, S., and Kim, W.: Time-advanced occurrence of moderate-size earthquakes in a stable intraplate region after a megathrust earthquake and their seismic properties, Sci. Rep., 8, 13331, https://doi.org/10.1038/s41598-018-31600- 5, 2018.

865   Hong, Y., OH J.-S., Hong S.-C., and Shin J.: Geomorphological Development and Fault Activity of the Central-Southern Yangsan Fault (I): Developmental Characteristics and Distribution of the Quaternary Landforms, J. Korean Geomorphological Assoc., 28, 67-81. https://doi.org/10.16968/JKGA.28.1.67, 2021.

Hough, S., and Page, M.: Toward a consistent model for strain accrual and release for the New Madrid seismic zone, central United States, *J. Geophys. Res.*, 116, B03311. http://dx.doi.org/10.1029/2010JB007783, 2011.

870   Hough, S.E., Armbruster, J.G., Seeber, L., and Hough, J.F.: On the modified Mercalli intensities and magnitudes of the 1811–1812 New Madrid earthquakes, J. Geophys. Res., 105(B10), 23,839–23,864, https://doi.org/10.1029/2000JB900110, 2000.

Hwang, B.-H., Lee, J. D., and Yang, K.: Petrological study of the granitic rocks around the Yangsan Fault: Lateral displacement of the Yangsan Fault, J. Geol. Soc. Korea, 40, 161–178, 2004.

Hwang, B. H., Lee, J. D., Yang, K., and McWilliams, M.: Cenozoic strike-slip displacement along the Yangsan Fault, southeast

875   Korean Peninsula, Int. Geol. Rev., 49, 768–775, https://doi.org/10.2747/0020-6814.49.8.768, 2007a.

Hwang, B. H., McWilliams, M., Son, M., and Yang, K.: Tectonic implication of A-type granites across the Yangsan Fault, Gigye and Gyeongju areas, southeast Korean Peninsula, Int. Geol. Rev., 49, 1094–1102, https://doi.org/10.2747/0020-6814.49.12.1094, 2007b.

Ikeya, M., Miki, T., and Tanaka, K.: Dating of a Fault by Electron Spin Resonance on Intrafault Materials, Science, 215, 1392-

880   1393, https://doi.org/10.1126/science.215.4538.1392, 1982.

Jin, K., Kim, Y.-S., Kang, H.C. and Shin, H.C.: Study on developing characteristics of the Quaternary Gusan Fault in Uljin, Gyeongbuk, Korea, J. Geol. Soc. Korea, 49, 197-207, https://doi.org/10.14770/jgsk.2013.49.2.197, 2013.

Johnston, A.C., and Schweig, E.S.: The enigma of the New Madrid earthquakes of 1811–1812, Annu. Rev. Earth Pl. Sc., 24, 339-384, https://doi.org/10.1146/annurev.earth.24.1.339, 1996.

885   Kanamori, H.: The energy release in great earthquakes, J. Geophys. Res., 82, 2981–2987, https://doi.org.10.1029/JB082i020p02981, 1977.

Kang, H.-C., Cheon, Y., Ha, S., Seo, K., Kim, J.-S., Shin, H. C., and Son, M.: Geology and U-Pb Age in the Eastern Part of Yeongdeok-gun, Gyeongsangbuk-do, Korea, *J. Petrological Soc. Korea, 27*, 153-171, https://doi.org/10.7854/JPSK.2018.27.3.15, 2018.

890   Kee, W.-S., Kim, Y.-H., Lee, H.-J., Choi, D.-L., Kim, B.-C., Song, K.-Y., Koh, H.-J., Lee, S.R., Yeon, Y.G., Hwang, S.-H., Sung, N.-H.: South eastern fault variable research and DB Construction, Korea Institute of Geoscience and Mineral Resources, Daejeon, 327 pp., 2009.

Khromovskikh, V. S.: Determination of magnitudes of ancient earthquakes from dimensions of observed seismodislocations, Tectonophysics, 166, 269-280, https://doi.org/10.1016/0040-1951(89)90219-9, 1989.

895   Kim, C.-M., Cheon, Y., Lee, T.-H., Choi, J.-H., Ha, S., and Jeong, J. O.: Long-Term Weakening Processes and Short-Term Seismic Slip Behavior of an Intraplate Mature Fault Zone: A Case Study of the Yangsan Fault, SE Korea, J. Geophys. Res-Sol Ea, 127, e2021JB023154, https://doi.org/10.1029/2021JB023154, 2022.

Kim, C.-M., Ha, S., and Son, M.: Evidence of coseismic slip recorded by Quaternary fault materials and microstructures, Naengsuri, Pohang, J. Geol. Soc. Korea, 56, 175-192, https://doi.org/10.14770/jgsk.2020.56.2.175, 2020a.

900   Kim, C.-M., Jeong, J. O., Gu, D., and Han, H.: Identification of materials in principal slip zones of faults by X-ray diffraction analysis using a small amount of sample, J. Geol. Soc. Korea, 53, 873-883, http://doi.org/10.14770/jgsk.2017.53.6.873, 2017a.

Kim, D.-E., and Seong. Y.B.: Cumulative Slip Rate of the Southern Yangsan Fault from Geomorphic Indicator and Numerical Dating, J. Kor. Geogr. Soc., 56, 201-213. https://doi.org/10.22776/KGS.2021.56.2.201, 2021.

Kim, D. E., and Oh. J.-S.: Landform Classification Using Geomorphons on the Middle Yangsan Fault System, Southeastern

905   Korea, J. Korean Geogr. Soc., 54, 493-505, 2019.

Kim, D.H., Hwang, J.H., Park, K.H., and Song, K.Y.: Explanatory Note of The Pusan Sheet, 1:1:250,000, Korea Institute of Energy and Resources, Daejeon, 1998.

Kim, H.-U., and Bae, T.-S.: Monitoring of Possible Activities of Yangsan Fault Zone Using GNSS, Appl. Sci., 13, 1862, https://doi.org/10.3390/app13031862, 2023.

910   Kim, I.-S.: Origin and tectonic evolution of the East Sea (Sea of Japan) and the Yangsan fault system: a new synthetic interpretation, J. Geol. Soc. Korea, 28, 84-109, 1992.

Kim, K.-H., Ree, J.-H., Kim, Y., Kim, S., Kang, S.Y., and Seo, W.: Assessing whether the 2017 M_w 5.4 Pohang earthquake in South Korea was an induced event, Science, 360, 1007-1009, https://doi.org/10.1126/science.aat6081, 2018.

Kim, K.-H., Seo, W., Hang, J., Kwon, J., Kang, S.Y., Ree, J.-H., Kim, S., and Liu, K.: The 2017 M_L 5.4 Pohang earthquake

915   sequence, Korea, recorded by a dense seismic network, Tectonophysics, 774, 228306, https://doi.org/10.1016/j.tecto.2019.228306, 2020b.

Kim, M.-C., Jung, S., Yoon, S., Jeong, R.-Y., Song, C.W., and Son, M.: Neotectonic crustal deformation and current stress field in the Korean Peninsula and Their Tectonic Implications: a review, J. Petrological Soc. Korea, 25, 169–193, https://doi.org/10.7854/JPSK.2016.25.3.169, 2016.

920   Kim, M.-J., and Lee, H.-K.: Long-term patterns of earthquakes influenced by climate change: Insights from earthquake recurrence and stress field changes across the Korean Peninsula during interglacial periods, Quaternary Sci. Rev., 321, 108369, https://doi.org/10.1016/j.quascirev.2023.108369, 2023

Kim, M.-J., and Lee, H.-W.: ESR dating of fault gouge - review, J. Geol. Soc. Korea, 56, 175-192, https://doi.org/10.14770/jgsk.2020.56.2.211, 2020.

925   Kim, N., Choi, J.-H., Park, S.-I., Lee, T.-H. and Choi, Y.: Cumulative offset analysis of the Central-Southern Yangsan Fault based on topography of Quaternary fluvial terrace, J. Geol. Soc. Korea, 56, 135-154, https://doi.org/10.14770/jgsk.2020.56.2.135, 2020c.

Kim, N., Park, S.-I., and Choi, J.-H.: Internal architecture and earthquake rupture behavior of a long-lived intraplate strike–slip fault: A case study from the Southern Yangsan Fault, Korea, Tectonophysics, 816, 229006, https://doi.org/10.1016/j.tecto.2021.229006, 2021.

Kim, T., Choi, J.-H., Cheon, Y., Lee, T.-H., Kim, N., Lee, H., Kim, C.-M., Choi, Y., Bae, H., Kim, S.-G., Ryoo, C.-R., and Klinger, Y.: Correlation of paleoearthquake records at multiple sites along the southern Yangsan Fault, Korea: Insights into rupture scenarios of intraplate strike-slip earthquakes, Tectonophysics, 854, 229817, https://doi.org/10.1016/j.tecto.2023.229817, 2023.

Kim, Y.-S. and Jin, K.: Estimated earthquake magnitude from the Yugye Fault displacement on a trench section in Pohang, SE Korea, J. Geol. Soc. Korea, 42, 79-94, 2006.

Kim, Y.-S., Jin, K., Choi, W.-H., and Kee, W.-S.: Understanding of active faults: A review for recent researches, J. Geol. Soc. Korea. 47, 723-752, 2011a.

Kim, Y.-S., Kihm, J.-H., and Jin, K.: Interpretation of the rupture history of a low slip-rate active fault by analysis of progressive displacement accumulation: an example from the Quaternary Eupcheon Fault, SE Korea, J. Geol. Soc., 168, 273–288, https://doi.org/10.1144/0016-76492010-088, 2011b.

Kim, Y.-S., Kim, T., Kyung, J. B., Cho, C. S., Choi, J.-H., Choi, C. U.: Preliminary study on rupture mechanism of the 9.12 Gyeongju Earthquake, J. Geol. Soc. Korea, 53, 407-422, https://doi.org.10.14770/jgsk.2017.53.3.407, 2017b.

Ko, K., Choi, S.-J., Lee, T.-H., Gihm, Y. S., Kim, C.-M., Kim, K., and Cheon, Y.: A multidisciplinary approach to characterization of the mature northern Yangsan fault in Korea and its active faulting, Mar. Geophys. Res., 43, 21, https://doi.org/10.1007/s11001-022-09486-w, 2022.

Korea Meteorological Administration: 2022 yearbook, Korea Meteorological Administration, Seoul, 416 pp., 2022. Retrieved from https://www.kma.go.kr (archived on 6/March/2023).

Kreutzer, S.: calc_FadingCorr(): Apply a fading correction according to Huntley and Lamothe (2001) for a given g-value and a given tc. Function version 0.4.3, in Luminescence, edited by Kreutzer, S., Burow, C., Dietze, M., Fuchs, M.C., Schmidt, C., Fischer, M., Friedrich, J., Mercier, N., Philippe, A., Riedesel, S., Autzen, M., Mittelstrass, D., Gray, H.J., and Galharret, J., Comprehensive Luminescence Dating Data Analysis R package version 0.9.23, available at https://CRAN.R-project.org/package=Luminescence (last access: January 2024), 2023.

Kyung, J. B.: Paleoseismological study and evaluation of maximum earthquake magnitude along the Yangsan and Ulsan Fault Zones in the Southeastern Part of Korea, Geophysics Geophys. Explor., 13, 187-197, 2010.

Kyung, J.B.: Paleoseismology of the Yangsan Fault, southeastern part of the Korean Peninsula, Ann. Geophys., 46, 983-996, http://hdl.handle.net/2122/999, 2003.

Lal, D.: Cosmic ray labeling of erosion surfaces: in situ nuclide production rates and erosion models, Earth Planet. Sc. Lett., 104, 424–439, https://doi.org/10.1016/0012-821X(91)90220-C, 1991.

960   Lee, C. H., Seong Y. B., Oh, J.-S., Kim. D. E.: Tectonic Geomorphology on Yugye-Bogyeongsa Area of Yangsan Fault Zone, J. Korean Geomorphological Assoc., 26, 93-106, https://doi.org/10.16968/JKGA.26.1.93, 2019.

Lee, H.-K., and Schwarcz, H. P.: ESR dating of the subsidiary faults in the Yangsan Fault System, Korea, Quaternary Sci. Rev., 20, 999–1003, https://doi.org/10.1016/S0277-3791(00)00055-X, 2001.

Lee, H.K., and Yang, J.S.: ESR dating of the Eupchon fault, south Korea, Quat. Geochronol., 2, 392–397,
965   https://doi.org/10.1016/j.quageo.2006.04.009, 2003.

Lee, J., Rezaei, S., Hong, Y., Choi, J.-H., Choi, J.-H., Choi, W.-H., Rhee, K.-W., and Kim, Y.-S.: Quaternary fault analysis through a trench investigation on the northern extension of the Yangsan fault at Dangu-ri, Gyungju-si, Gyeongsangbuk-do, J. Geol. Soc. Korea, 51, 471-485, https://doi.org.10.14770/jgsk.2015.51.5.471, 2015.

Lee, K.: Historical earthquake data of Korean. J. Korea Geophys. Soc. 1, 3-22, 1998.

970   Lee, K., and Yang, W.-S.: Historical Seismicity of Korea, B.Seismol. Soc. Am., 96, 846-855, https://doi.org/10.1785/0120050050, 2006.

Lee, S.: Characteristics of the Quaternary Faults in SE Korea: Insight from the Yangsan Fault and Gokgang Fault, Ph.D. thesis, Pusan National University, Korea, 184 pp., 2023.

Lee, S., Han, J., Ha, S., Lim, H., Seong, Y. B., Choi, J.-H., Lee, C. H., Kim, S.-J., Kang, H.-C., Kim, M.-C., Lim, H., and Son,
975   M.: Characteristics of the Quaternary faulting detected along the Yangsan Fault in Yugye- and Jungsan-ri, northern Pohang City, J. Geol. Soc. Korea, 58, 427-443, http://doi.org.10.14770/jgsk.2022.58.4.427, 2022.

Lee, Y., Cheon, Y., Ha, S., Kang, H.-C., Choi, J.-H., and Son, M.: Geometric and kinematic characteristics of the Quaternary fault at Seooe site, in Goseong-gun, Gyeongsangnam-do, J. Geol. Soc. Korea, 53, 115-127, https://doi.org/10.14770/jgsk.2017.53.1.115, 2017.

980   Lim, H., Ha, S., Ryoo, C.-R., Lee, T.-H., and Son, M.: Evidence of surface rupture in the southernmost part of the Yangsan fault and deterministic seismic hazard assessment: in the Busan metropolitan area, in: 76th Annual Meeting of the Geological Society of Korea and 2021 Fall Joint Conference of the Geological Sciences, Jeju, Korea, 26-28 October 2021, 275, 2021.

Liu, J., Ren, Z., Min, W., Ha, G., and Lei, J.: The advance in obtaining fault slip rate of strike slip fault-A review. Earthq. Res. Adv., 1, 100032. https://doi.org/10.1016/j.eqrea.2021.100032, 2021.

985   Liu, M., and Stein, S.: Mid-continental earthquakes: Spatiotemporal occurrences, causes, and hazards, Earth-Sci. Rev., 162, 364–386, https://doi.org/10.1016/j.earscirev.2016.09.016, 2016.

Mason, D.B.: Earthquake magnitude potential of the Intermountain Seismic Belt, USA, from surface-parameter scaling of late Quaternary faults. B. Seismol. Soc. Am., 86, 1487–1506, https://doi.org/10.1785/BSSA0860051487, 1996.

McCalpin, J.P.: Application of Paleoseismic Data to Seismic Hazard Assessment and Neotectonic Research, in:
990   Paleoseismology, 2nd ed., edited by McCalpin, J.P., Academic Press-Elsevier, Burlington, USA, 1–106, https://doi.org/10.1016/S0074-6142(09)95009-4, 2009.

Min, Z., Hu, G., Jiang, X., Liu, S., and Yang, Y.: Catalog of Chinese Historic Strong Earthquakes From 23 AD to 1911, Seismological Press, Beijing, China, 514 pp., 1995.

Murray, A. S., and Wintle, A. G.: Luminescence dating of quartz using an improved single-aliquot regenerative-dose protocol, Radiat. Meas., 32, 57-73, https://doi.org/10.1016/S1350-4487(99)00253-X, 2000.

Murray, J., and Langbein, J.: Slip on the San Andreas Fault at Parkfield, California, over Two Earthquake Cycles, and the Implications for Seismic Hazard, B.Seismol. Soc. Am., 96, S283–S303, https://doi.org/10.1785/0120050820, 2006.

O'Neill, C., Müller, D., and Steinberger, B.: On the uncertainties in hot spot reconstructions and the significance of moving hot spot reference frames, Geochem. Geophy. Geosy., 6, https://doi.org/10.1029/2004GC000784, 2005.

Obara, K., and Kato, A.: Connecting slow earthquakes to huge earthquakes. Science, 353, 6296, https://doi.org/10.1126/science.aaf1512, 2016.

Park, C., and Lee, G.: Analysis on Fault-Related Landforms in the Gyeongju Area of the Yangsan Fault Valley, J. Korean Geomorphological Assoc., 25, 19-30, https://doi.org.-/10.16968/JKGA.25.1.19, 2018.

Park, Y., Ree, J.-H., and Yoo, S.-H.: Fault slip analysis of Quaternary faults in southeastern Korea, Gondwana Res., 9, 118–125, https://doi.org/10.1016/j.gr.2005.06.007, 2006.

Powell, R. E., and Weldon II, R. J.: Evolution of the San Andreas fault, Annu. Rev. Earth Pl. Sc., 20, 431-468, https://doi.org/10.1146/annurev.ea.20.050192.002243, 1992.

Reimer, P., Austin, W., Bard, E., Bayliss, A., Blackwell, P., Bronk Ramsey, C., and Talamo, S.: The IntCal20 Northern Hemisphere Radiocarbon Age Calibration Curve (0–55 cal kBP), Radiocarbon, 62, 725–757, https://doi.org/10.1017/RDC.2020.41, 2020.

Reiter, L.: Earthquake Hazard Analysis: Issue and Insights. Columbia University Press, New York, USA, 254 pp., 1990.

Ryoo, C.-R., and Cheon, Y.: Characteristics of the Main Fault Zone Developed Along Yangsan Fault: On the Outcrop of Cheonjeon-ri, Dudong-myeon, Ulju-gun, Ulsan, Korea, J. Petrological Soc. Korea, 28, 347-357, https://doi.org/10.7854/JPSK.2019.28.4.347, 2019.

Ryoo, C.-R., Lee, B.-J., Cho, D.-L., Chwae, U.-C., Choi, S.-J., and Kim J.-Y.: Quaternary fault of Dangu-ri in Gyeongju Gangdong-myeon: Byeokgye Fault, in: Spring Joint Conference on East-North Asia Ore deposit of Cause of Formation, The Korean Society of Economic and Environmental Geology/The Korean Society of Mineral and Energy Resources Engineers/Korean Society of Earth and Exploration Geophysicists, 1999.

Sadler, P.: The Influence of Hiatuses on Sediment Accumulation Rates, GeoResearch Forum, 5, 15-40, 1999.

Schellart, W. P., and Rawlinson, N.: Convergent plate margin dynamics: New perspectives from structural geology, geophysics and geodynamic modelling, Tectonophysics, 483, 4-19, https://doi.org/10.1016/j.tecto.2009.08.030, 2010.

Seno, T., Sakurai, T., and Stein, S.: Can the Okhotsk plate be discriminated from the North American plate?, J. Geophys. Res.-Sol. Ea., 101(B5), 11305-11315, https://doi.org/10.1029/96JB00532, 1996.

Seno, T., Stein, S., and Gripp, A. E.: A model for the motion of the Philippine Sea plate consistent with NUVEL-1 and

1025   geological data, J. Geophys. Res.- Sol. Ea., 98(B10), 17941-17948, https://doi.org/10.1029/93JB00782, 1993.

Shimazaki, K., and Nakata, T.: Time-predictable recurrence model for large earthquakes, Geophys. Res. Lett., 7, 279-282, https://doi.org/10.1029/GL007i004p00279, 1980.

Sim, H., Song, Y., Son, M., Park, C., and Choi, W.: Reactivated Timings of Yangsan Fault in the Northern Pohang Area, Korea, Econ. Environ. Geol., 50, 97-104, https://doi.org/10.9719/EEG.2017.50.2.97, 2017.

1030   Smith, B. R., and Sandwell, D. T.: A model of the earthquake cycle along the San Andreas Fault System for the past 1000 years, J. Geophys. Res., 111, B01405. https://doi.org/10.1029/2005JB003703, 2006.

Sohn, D.-H., Choi, B.-K., Kim, S., Park, S.-C., Lee, W.-J., and Park, P.-H.: Decaying Post-Seismic Deformation Observed on the Korean Peninsula Following the 2011 Tohoku-Oki Earthquake, Sensors, 21, 4493, https://doi.org/10.3390/s21134493, 2021.

1035   Son, M., Song, C.W., Kim, M.-C., Cheon, Y., Cho, H., and Sohn, Y.K.: Miocene tectonic evolution of the basins and fault systems, SE Korea: dextral, simple shear during the East Sea (Sea of Japan) opening, J. Geol. Soc. London, 172, 664-680, https://doi.org/10.1144/jgs2014-079, 2015.

Song, C.W.: Study on the evolution of the Miocene Pohang Basin based on its structural characteristics, Ph.D. thesis, Pusan National University, Korea, 146 pp., 2015.

1040   Song, Y., Ha, S., Lee, S., Kang, H.-C., Choi, J.-H., and Son, M.: Quaternary structural characteristics and paleoseismic interpretation of the Yangsan Fault at Dangu-ri, Gyeongju-si, SE Korea, through trench survey, *J. Geol.Soc. Korea, 56*, 155–173, https://doi.org/10.14770/jgsk.2020.56.2.155, 2020.

Song, Y., Park, C., Sim, H., Choi, W., and Son, M.: Reactivated Timings of Yangsan Fault in the Sangcheon-ri Area, Korea, Econ. Environ. Geol., 49, 97-104, https://doi.org/10.9719/EEG.2016.49.2.97, 2016.

1045   Song, Y., Sim, H., Hong, S., and Son, M.: K-Ar Age-dating Results of Some Major Faults in the Gyeongsang Basin: Spatio-temporal Variability of Fault Activations during the Cenozoic Era, Econ. Environ. Geol., 52, 449-457, https://doi.org/10.9719/EEG.2019.52.5.449, 2019.

Talwani, P.: On the nature of intraplate earthquakes, J. Seismol., 21, 47-68, https://doi.org/10.1007/s10950-016-9582-8, 2017.

Uchida, N., and Burgmann, R.: Repeating Earthquakes, Annu. Rev. Earth Pl. Sc., 47, 305–332, 1050   https://doi.org/10.1146/annurev-earth-053018-060119, 2019.

Wells, D. L., and Coppersmith, K. J.: New empirical relationships among magnitude, rupture length, rupture width, rupture area, and surface displacement, B. Seismol. Soc. Am., 84, 974–1002, https://doi.org/10.1785/BSSA0840040974, 1994.

Williams, R.T., Goodwin, L.B., Sharp, W.D. and Mozley, O.S.: Reading a 400,000-year record of earthquake frequency for an intraplate fault, P. Natl. Acad. Sci. USA, 114, 4893–4898. https://doi.org/10.1073/pnas.1617945114, 2017.

1055   Woith, H., Petersen G.M., Hainzl, S., and Dahm, T.: Review: Can Animals Predict Earthquakes?, B. Seismol. Soc. Am., 108, 1031–1045, https://doi.org/10.1785/0120170313, 2018.

Wolin, E., Stein, S., Pazzaglia, F., Meltzer, A., Kafka, A., and Berti, C.: Mineral, Virginia, earthquake illustrates seismicity of a passive-aggressive margin, Geophys. Res. Lett., 39, L02305, https://doi.org/10.1029/2011GL050310, 2012.

Woo, S., Lee, H., Han,R., Chon, C.-M., Son, M., and Song, I.: Frictional properties of gouges collected from the Yangsan Fault, SE Korea. J. Geol. Soc. Korea, 51, 569-584, https://doi.org//10.14770/jgsk.2015.51.6.569, 2015.

Wyss, M.: Cannot Earthquakes Be Predicted?, Science, 278, 487-490, https://doi.org/10.1126/science.278.5337.48, 1997.

Xu, S., Nieto-Samaniego, A.F., and Alaniz-Àlvarez, S.A.: Quantification of true displacement using apparent displacement along an arbitrary line on a fault plane, Tectonophysics, 467, 107-118, https://doi.org/10.1016/j.tecto.2008.12.004, 2009.

Yang, J.-S., and Lee, H.-K.: ESR dating of fault gouge from the Gacheon 1 site on the Yangsan fault zone, J. Geol. Soc. Korea, 48, 459-472, 2012.

Yang, J.-S., and Lee, H.-K.: Quaternary Fault Activity of the Yangsan Fault Zone in the Samnam-myeon, Ulju-gun, Ulsan, Korea, Econ. Environ. Geol., 47, 17-27, https://doi.org/10.9719/EEG.2014.47.1.17, 2014.

1060

1065